

Formation of epizonal gold mineralization within the Latimojong Metamorphic Complex, Sulawesi, Indonesia: Evidence from mineralogy, fluid inclusions and Raman spectroscopy



Andy Yahya Al Hakim^{a,b,*}, Frank Melcher^a, Walter Prochaska^a, Ronald Bakker^a, Gerd Rantitsch^a

^a Department of Applied Geosciences and Geophysics, Montanuniversität Leoben, Peter Tunner Strasse 5, 8700 Austria

^b Research Group of Earth Resources Exploration, Faculty of Mining and Petroleum Engineering, Bandung Institute of Technology, Ganesha 10, Bandung, 40132, Indonesia

ARTICLE INFO

Keywords:

Orogenic gold
Fluid inclusions
Raman spectroscopy of carbonaceous material
Awak Mas
Salu Bullo

ABSTRACT

The gold deposits within the Latimojong Metamorphic Complex of Sulawesi, Indonesia, including Awak Mas and Salu Bullo, are estimated to host 50 tonnes Au with an average grade of 1.41 g/t. They are located within the metamorphic basement consisting of pumpellyite- to greenschist-facies metasedimentary and metavolcanic rocks, where gold precipitated in quartz veins that fill north-south striking normal faults and extensional fractures. The mineral assemblage is dominated by pyrite, chalcopyrite, galena, minor tetrahedrite-tennantite and sphalerite; gold is electrum with a low silver content (Au:Ag ratio of 8.5 to 9.1). Albite, dolomite-ankerite, siderite, chlorite, and white mica are the main alteration minerals. Quartz, albite and carbonate veins hosting H₂O-bearing fluid inclusions with minor aqueous-carbonic phases (CO₂ ± N₂) were detected (mole fraction < 0.15). Raman microspectroscopy, microthermometry, and crush leach analysis of gold-bearing quartz veins and associated host rocks provide evidence for processes resembling those described for epizonal gold mineralization. The gold bearing fluids have salinities between 1.4 and 7.3 eq. mass% NaCl and were trapped in quartz at about 180–250 °C and < 1.27 kbar, corresponding to depths less than 5 km. Trapping conditions of barren veins are about 190–390 °C and < 1.15 kbar with salinities ranging from 2.2 and 6.1 eq. mass% NaCl. Halogen and alkali ratios (Na/Cl/Br/I) from crush leach analyses correspond to deposits originating from metamorphic fluids with a strong albitization signature during ore formation. Isothermal decompression during the retrogression stage mobilized large volumes of fluids, leading to significant gold mineralization within the Awak Mas District.

1. Introduction

The Cretaceous Latimojong Metamorphic Complex (LMC) of Sulawesi, Indonesia, is host to several gold deposits. These include the Awak Mas, Salu Bullo, Tarra, and other satellite prospects (collectively referred to as the Awak Mas District, [Querubin and Walters, 2012](#)), with total indicated and inferred resources of 38.4 Mt at 1.41 g/t Au ([Cube, 2017](#)). There have been numerous models for the origin of the Awak Mas District, including orogenic gold deposit models ([Hakim, 2017](#); [Hakim et al., 2017](#); [Hakim and Melcher, 2017b, 2016b, 2015](#); [Harjanto, 2017](#); [Harjanto et al., 2016a,b](#); [Harjanto et al., 2015](#); [Querubin and Walters, 2012](#); [Tuakia et al., 2016](#)). Several authors also invoked the role of intrusions and suggested a genetic model for intrusion-related gold deposits ([Archibald et al., 1996](#); [Meyer, 2016](#); [van Leeuwen and Pieters, 2011](#)). The most recent feasibility study also considered a high

level, low-sulphidation epithermal system ([Cube, 2017](#)). Despite the fact that a number of studies have been undertaken in the Awak Mas District, many questions remain unanswered. These include the role of fluids in gold precipitation, the metamorphic history, the genetic model and timing of mineralization.

Raman spectroscopy is an effective method to calculate the evolution of carbonaceous material (CM) during regional metamorphism ([Beyssac et al., 2002](#); [Lünsdorf, 2015](#); [Rantitsch et al., 2004](#)). During metamorphism, CM transforms to anthracite, meta-anthracite, semi-graphite and graphite ([Kwiecińska and Petersen, 2004](#); [Rantitsch et al., 2016](#)). Such materials are commonly associated with gold deposits in metamorphic basement, i.e. the Otago-Alpine Schists and the Macraes orogenic gold deposits, New Zealand ([Craw and MacKenzie, 2016](#); [Hu et al., 2015](#); [Pitcairn et al., 2005](#)) and the Suurikuusikko gold deposit-Kittilä, Northern Finland ([Wyche et al., 2015](#)). The presence of CM in

* Corresponding author at: Research Group of Earth Resources Exploration, Faculty of Mining and Petroleum Engineering, Bandung Institute of Technology, Ganesha 10, Bandung, 40132, Indonesia.

E-mail address: andyahya@mining.itb.ac.id (A.Y.A. Hakim).

<https://doi.org/10.1016/j.oregeorev.2018.05.001>

Received 9 January 2018; Received in revised form 29 April 2018; Accepted 1 May 2018
0169-1368/ © 2018 Elsevier B.V. All rights reserved.

organic-matter (OM)-rich shales can contribute to the sequestration of metals during sediment dewatering and ore deposition, because CM act as sources for metals during subsequent metamorphic processes (Hu et al., 2015; Large et al., 2011). Alternatively, CM may also form from hydrothermal fluids containing volatile organic compounds during gold deposit formation (Craw, 2002; Gu et al., 2012). However, links between Raman spectra of carbonaceous material, pressure-temperature-depth estimation and the gold mineralization processes have received less attention.

It is the aim of this paper to use a combination of Raman and petrographic analysis to document the metamorphic temperature-pressure evolution within the LMC. We present results of a detailed investigation of the ore-related mineral assemblages and the fluid inclusion data characterizing the fluids involved in ore precipitation. Crush leach analysis of quartz, carbonate and electron microprobe analysis of chlorite and mica provide an insight into the physical and chemical factors controlling the ore-forming processes. The objectives of this paper are (i) to trace the origin of ore-forming fluids, (ii) to construct a genetic model for the development of gold mineralization, and (iii) to reconstruct the metamorphic and post-metamorphic *P-T* path of the ore-hosting formation.

2. Geological setting

The Latimojong Metamorphic Complex (LMC, Fig. 1) is situated in the Western Sulawesi arc, as part of a Late Cretaceous accretionary complex (van Leeuwen and Muhandjo, 2005; Wakita, 2000; White et al., 2017). It consists of moderately to strongly folded metamorphic rocks (phyllite, chlorite schist, metasandstone), tectonically mixed with volcanic rocks (metamafic, volcanoclastic rocks) (Fig. 1b-c). Limited paleontological and radiometric data and comparison with the Bantimala and Barru metamorphic complexes (South Sulawesi) suggest that the sedimentary protoliths of the LMC formed in the Early Cretaceous and accreted to the Sundaland margin in the mid-Cretaceous (White et al., 2017), when the complex was deformed, underwent partly high-pressure metamorphism and became uplifted above sea level before the Eocene (Bergman et al., 1996; Parkinson, 1998; White et al., 2017).

Electron microprobe analyses of clinopyroxene and chromian spinel phenocrysts hosted by metamafic and metatuffite in the LMC and whole rock analyses by XRF and ICP-MS indicate a strong island-arc basalt affinity (Hakim, 2017). In multi-element spider diagrams, these mafic metavolcanic rocks show an extreme enrichment of Pb, Large Ion Lithophile Elements (LILE, i.e. Cs, Rb, Ba) with respect to High Field Strength Elements (HFSE, including Nb, Ta, Ti, P), Light REE (LREE, i.e. La, Ce, ...) and Heavy REE (HREE, i.e., Yb, Lu, ...). The protolith of these rocks appears to be equivalent to eclogites and blueschists of Bantimala, South Sulawesi, part of the thicker-crust environments (Oceanic Island Basalt-OIB or Island Arc Basalt-IAB) that were subducted under the southeast margin of Sundaland Craton (Maulana et al., 2013; Parkinson et al., 1998; Wakita et al., 1996).

The topography in the Awak Mas District is moderately to extremely rugged, ranging from 800 to 1400 m above sea level. The highest level in close proximity to the area of Awak Mas is the summit of Mount Rantemario (3478 m above sea level) on the Western margin of the project area. Slope gradients are steepest within the southern to western portions grading to moderate towards the northern and eastern sections. Dense primary forest exists in the northern region and is generally less accessible in regions of higher elevation. Major drainage systems are Salu Siwa, Salu Lombok, and Salu Tolobo. The Salu Siwa is the most dominant river and forms a north-south trending valley that appears to coincide with a major suture zone dividing the Eastern Latimojong sequence from the Lamasi Complex (Fig. 1b-c).

The Lamasi Complex, part of the East Sulawesi Ophiolite (ESO) (Bergman et al., 1996; Kadarusman et al., 2004; Parkinson, 1998; White et al., 2017), is situated east of the LMC (Fig. 1b-c). It is composed of dioritic plutons, basaltic sheeted dykes, pillow lavas, greenstones and

tuff. The Lamasi Complex is intensely deformed, altered by ocean-floor metamorphism, and bounded by thrust faults. Generally, the mafic components of the Lamasi Complex have depleted Sr-Nd isotopes, MORB-like geochemistry, and possibly represent obducted MORB or back-arc oceanic crust (Bergman et al., 1996). Isotopic data (K-Ar, ⁴⁰Ar-³⁹Ar, Rb-Sr and Sm-Nd) suggest Cretaceous to Eocene formation ages (Bergman et al., 1996; Parkinson, 1998; Priadi et al., 1994). The ESO was obducted onto the Sundaland Craton at 30 Ma, based on a K-Ar age of the metamorphic sole (Parkinson, 1998). By contrast, White et al. (2017) suggested that the timing of ophiolite obduction was between Early to Middle Miocene, and the Lamasi Complex may represent Eocene-Oligocene arc/back-arc volcanic rocks.

The Late Cenozoic magmatism in Western Sulawesi has been the subject of much debate. The hypotheses proposed can be divided into two groups: (i) a collision event caused crustal/lithospheric thickening, followed by melting in the lower crust to give rise to magmatism (Bergman et al., 1996; Polve et al., 2001; Polvé et al., 1997; Priadi et al., 1994), and (ii) an extensional tectonic regime in the mid-Miocene causing asthenospheric mantle uprising, resulting in shoshonitic to ultrapotassic magmatism and CAK magmatism in Central West and North Western Sulawesi, underlain by a Cretaceous continental fragment and subjected to strong uplift in the Pliocene (Hall and Wilson, 2000; Maulana et al., 2016; van Leeuwen et al., 2010; White et al., 2017). Based on our fieldwork campaign and drill hole observations in the Awak Mas District, intrusive rocks within this complex are rare. Most of the rocks are metamorphosed and none of the above scenarios are supported by the outcrop evidence. Pumpellyite, epidote and actinolite observed in clinopyroxene-phyric metamafic and metatuffite from the Salu Bullo deposit are indicator minerals for high-pressure low-temperature metamorphism, and most likely represent subduction-related metamorphism processes during the Cretaceous (Hakim and Melcher, 2017a).

Soesilo (1998) distinguished three deformational phases in the Latimojong Mountains. (i) Initial deformation and metamorphism of siliciclastic, volcanic and carbonate rocks. Metamorphism in the zeolite to pumpellyite – actinolite facies reached temperatures of 310–350 °C and pressures of 3–4.5 kbar, corresponding to a depth of > 9 km. (ii) Ductile deformation, blueschist- to greenschist-facies metamorphism of metasedimentary and metavolcanic rocks, characterized by pumpellyite-actinolite and glaucophane in metavolcanic rocks. The estimated temperature and pressure of > 350 °C and > 6 kbar and further increased up to 550 °C in the low amphibolite facies (Soesilo, 1998). Final stage (iii) brittle deformation comprised the formation of chlorite and calcite as crack fillings.

During exploration work since the early 1990s in the LMC, more than a thousand drill-holes with a total aggregated length of 118,081 m yielded estimated total resources of 38.4 Mt (cut-off grade of 0.5 g/t) (One Asia Resources, 2017). Total gold contents of 50 tonnes at 1.41 g/t Au exceed the gold exploited in several historic gold mines in Indonesia (Garwin et al., 2005). Gold in the Awak Mas and Salu Bullo deposits (Fig. 1c) precipitated as laminated veins or lenses within oblique normal faults, extensional shears and fractures as well as in the host metasediments and metavolcanic rocks (Fig. 2). Early and late-mineral faulting dominates within the structures, with late-mineralization faults as host to the main veins.

The Awak Mas deposit (average grade 1.4 g/t) consists of five ore bodies dipping between 15° and 50° towards the north and dissected by three major N-S-trending faults. The ore bodies at Awak Mas can be traced along strike for up to 800 m and range from several meter up to 70 m thick (One Asia Resources, 2017). The mineralized zone cuts a metasedimentary sequence (phyllite, carbonaceous phyllite, chlorite schist; Fig. 3a-b) with associated brecciation and stockwork quartz vein development.

The Salu Bullo deposit, situated 2 km to the southeast of the Awak Mas deposit, is considered to be analogous to the Awak Mas deposit, but with a more dominant sub-vertical structural control. Accretion of

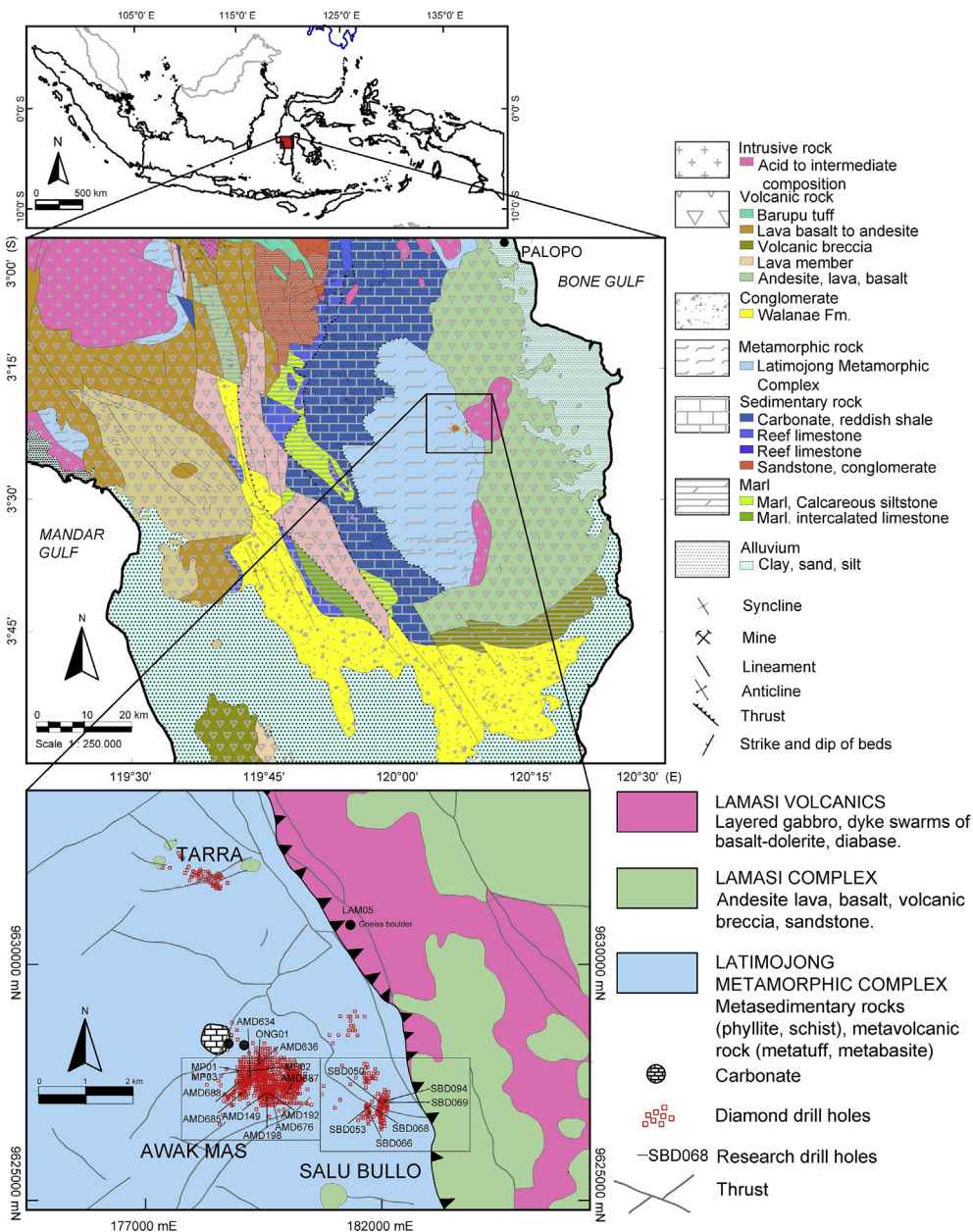


Fig. 1. (a) Simplified geological map of the Latimojong Metamorphic Complex and its surrounding (Djuri et al., 1988). Research area is highlighted by square. (b) General map of the Latimojong metamorphic complex in South Sulawesi with location of the studied ore deposits (modified after Archibald et al. 1996; One Asia Resources Limited, 2013).

ophiolite rocks onto metasedimentary sequences by the major, north-northwest striking Lamasi-Latimojong thrust are the main structural features in the Salu Bullo region. The host rocks are metamafic, meta-tuff, hematitic mudstone, with some relics of preserved magmatic minerals in metamafic (clinopyroxene, chromian spinel). Mafic metavolcanic rocks and hematite mudstone alteration are abundant in Salu Bullo and serve as important indicators to distinguish between the Awak Mas and Salu Bullo deposits.

The four ore bodies at Salu Bullo (Freddie, Bandoli, Biwa and Lelating veins) overprint ductile deformation and are related to (i) quartz vein stockworks and (ii) quartz – albite – pyrite – chlorite alteration. The Salu Bullo deposit has an average grade of 2.5 g/t, typically associated with pinch-and-swell vein systems varying in width between < 1 and 30 m, that are commonly parallel in fissures along a 1.5 km strike length. There are zones of carbonatization (siderite + ankerite), chloritization and albitization, with high Au/Ag ratio

(8.5:1 to 9:1) in gold based on electron microprobe observations (Hakim and Melcher, 2016a). Currently (early 2018) the gold project is in an advanced feasibility study stage.

3. Samples and methods

Representative vein and host rock samples from the Awak Mas and Salu Bullo deposits were collected from outcrops and twelve drill holes (Fig. 2 and Appendix A).

3.1. Petrography

Sixty-two polished thin sections of the the gold-bearing veins and their host rocks have been studied from the LMC and the overlying Lamasi Ophiolite unit. Petrographic descriptions of veins and host rocks were performed at the Chair of Resource Mineralogy,

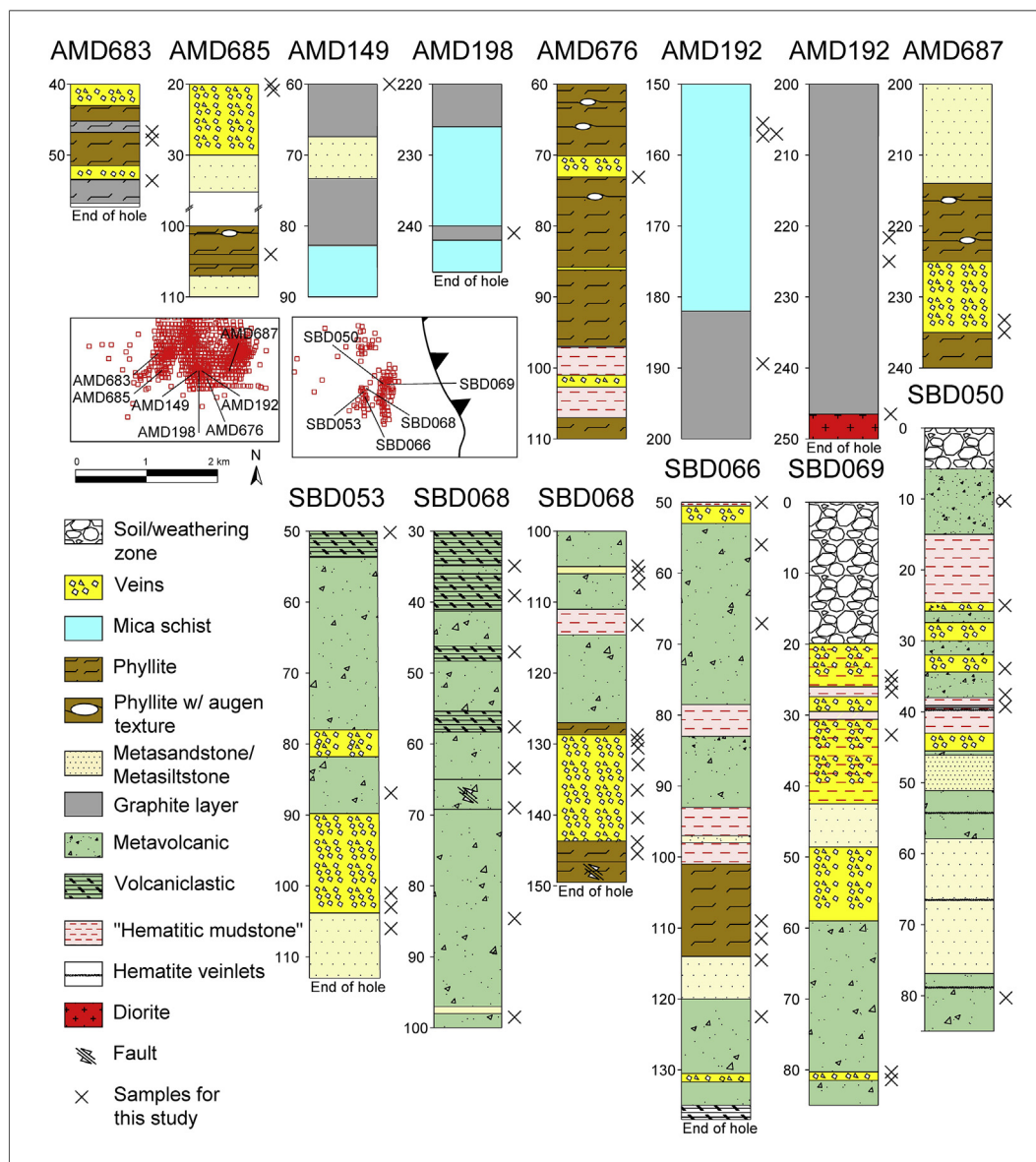


Fig. 2. Bore hole sample distribution used for this study.

Montanuniversität Leoben using an Olympus BX60 microscope. The mineralogical composition was determined using a scanning electron microscope ZEISS EVO MA 10 equipped with a secondary electron (SE) and a back-scattered electron (BSE) detector at the Chair of Geology and Economic Geology, Montanuniversität Leoben. The scanning electron microscope (SEM) was equipped with a BRUKER Nano Xflash 430 M energy dispersive X-ray (EDX) detector. The instrument operated at 15–20 keV accelerating voltage, a 30 μm aperture size and a 10–11 mm free working distance.

3.2. Electron microprobe analysis

The electron microprobe analyses were conducted using a JEOL JXA 8200 at the Chair of Resource Mineralogy, MU Leoben, to determine the chemical composition of chlorite and mica. The electron beam was set to 15 keV with 10 nA beam current and a beam diameter of 1 μm . The following diffracting crystals were selected: TAP for Na and Al; PETJ for Ca, Mg and Si; PETH for K; and LIFH for Fe, Ti and Mn. As a reference material for mica, sanidine is used for Na and K, albite for Al and Si, wollastonite for Ca, kaersutite for Mg, almandine for Fe, rutile for Ti, rhodonite for Mn. For chlorite, albite is used for Na and Al, wollastonite

for Ca, sanidine for K and Si, phlogopite for Mg, kaersutite for Fe, rutile for Ti, rhodonite for Mn and synthetic Cr_2O_3 for Cr. The acquisition time of analysis is 20 s for peak and 10 s for background. The Solaris system software provided by JEOL is used to perform the ZAF correction.

3.3. Raman spectroscopy on carbonaceous materials and fluid inclusions

Nine samples of carbonaceous material from graphitic schist and carbonaceous breccias (Table 1) were separated chemically from other mineral phases (Rantitsch et al., 2004). Raman measurements were performed using a Jobin Yvon LABRAM Raman microprobe using an Nd-YAG laser with the wavelength 532 nm and a 10x objective. To obtain a better signal to noise ratio, five scans with an acquisition time of 30 s in the 700–2000 cm^{-1} region were summed to a composite spectrum. Ten spectra were recorded for each sample. Numerical analysis of the Raman spectrum was performed using the fitting procedure of Lünsdorf et al. (2014).

Vapour and liquid phases of single inclusions within quartz were also analysed using the laser Raman probe. The laser spot on the samples was focused approximately to a diameter of one μm . For the

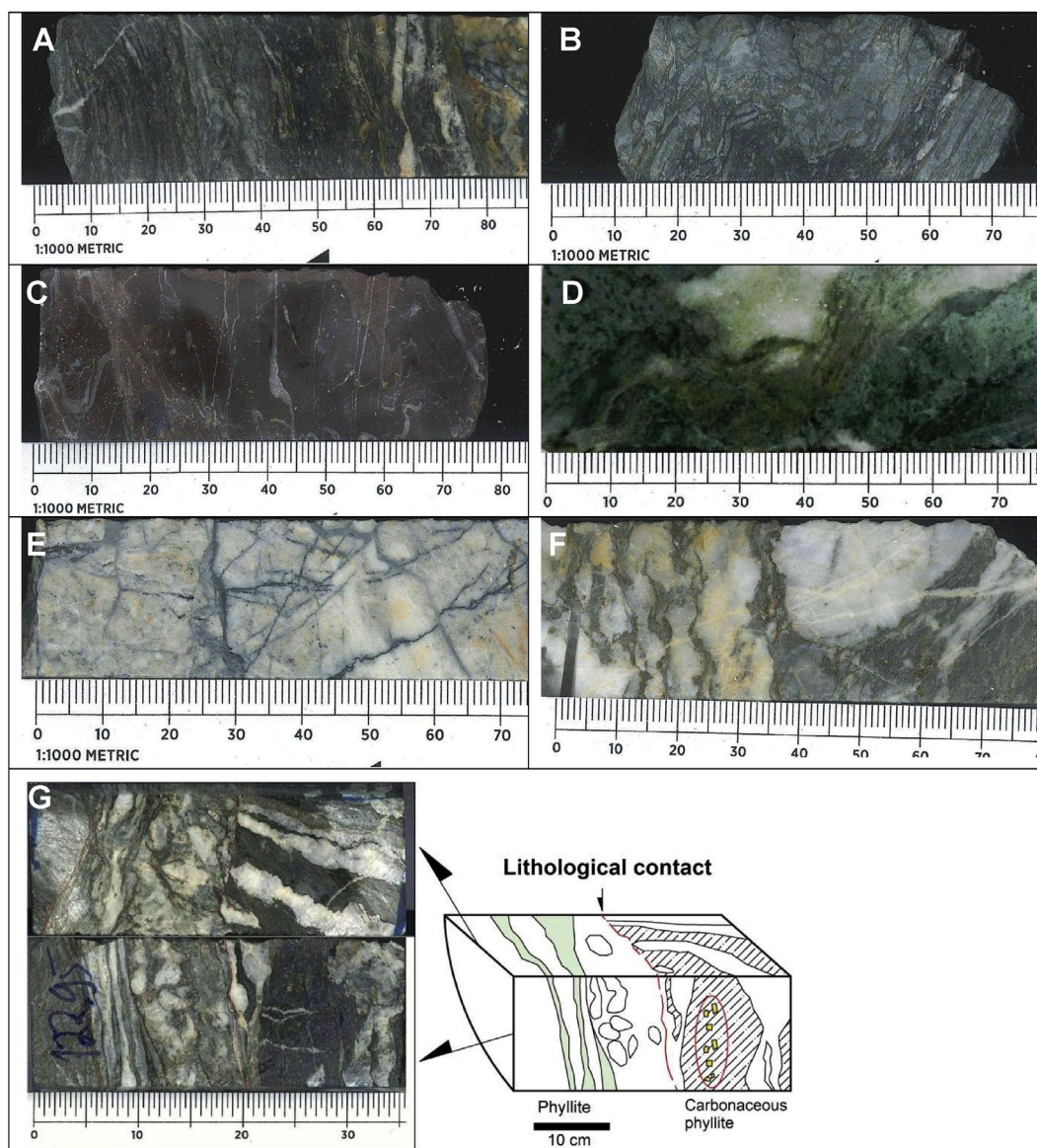


Fig. 3. Photographs of diamond drill core samples of the host rocks and mineralization. (a) Phyllite consisting of quartz – siderite – muscovite with carbonate alteration. This sample is mineralized with abundant sulphide and sulphosalt. (b) Carbonaceous phyllite composed of carbonaceous material, carbonate, quartz and albite. (c) Mineralized hematitic mudstone crosscut by late carbonate veinlets. Silica alteration. (d) Quartz veins with carbonate – albite alteration in metabasite. (e) Quartz – pyrite ± hematite veinlet in breccia veins. (f) Breccias composed of quartz clasts, containing coarse grained sulphides. (g) A photograph of lithological contact between phyllite and carbonaceous phyllite. Sulphides are abundant in graphite band.

analysis of CO_2 , N_2 , and CH_4 vapour phases, spectra were recorded from 1000 to 3800 cm^{-1} using a single 20-s integration time per spectrum. All inclusions for microthermometric analysis were observed carefully using Raman spectroscopy to confirm the composition of the vapour phases. Fityk 0.9.8 open-source software was used to deconvolve the Raman spectra of inclusions.

3.4. Microthermometry

Samples were taken from representative drill core profiles and outcrop through the ore zones. Twenty-two double-polished sections, which represent the various hydrothermal alteration systems with and without gold mineralization were examined petrographically, and of these nine samples were selected for microthermometric analysis (Appendix A).

A transmitted light microscope was used to obtain information on the relative formation chronology and paragenetic sequences of the FI.

Microthermometric data were collected using a Linkam THSMG 600 heating and freezing stage equipped with a microscope with objective magnification of $100\times$. Calibration was done by using synthetic fluid inclusions with a melting point of CO_2 at $-56.6\text{ }^\circ\text{C}$, the melting of water at $0.0\text{ }^\circ\text{C}$ and the critical homogenization temperature of water at $374.0\text{ }^\circ\text{C}$. The precision within the low temperature range is estimated to be $0.1\text{ }^\circ\text{C}$.

The volume fraction of fluid inclusions was determined by measuring the vapour bubble diameter at room temperature using the $100\times$ magnification objective lens. Calculation of perimeter and area of vapour was obtained by drawing the fluid inclusion along the perimeters of the inclusion and vapour bubble using ImageJ software (Bakker and Diamond, 2006). For optimal measurements, large, regular and near-surface inclusions were considered to minimize the error. For irregular shaped inclusions, volume fractions were calculated using the PVTX properties as an input of the BULK software (Bakker, 2003).

The software package CLATHRATES (Bakker, 1997) and FLUIDS

(version 1) (Bakker, 2003) were used to calculate fluid properties of fluid inclusions from Raman spectroscopy, microthermometry and volume fraction based on optical measurements. Program *ICE* from the package *CLATHRATES* (Bakker, 1997) was used to calculate bulk fluid properties at *QI* conditions based on $T_m(\text{ice})$, $T_m(\text{clathrate})$, gas composition and volume-fraction composition. The properties of low-density gas mixtures are calculated with the equations from Peng and Robinson (1976). Furthermore, the equation of state of Duan et al. (1995, 1992a,b) was selected for fugacity calculations in clathrate equilibrium. The isochores that result from the output of *ICE* and *BULK* software were further calculated using software *ISOC* (Bakker, 2003). The equations of state of Anderko and Pitzer (1993) and Duan et al. (1995) were used to calculate the isochores in the $\text{H}_2\text{O}-\text{CO}_2-\text{CH}_4-\text{NaCl}$ fluid system.

3.5. Crush leach analysis on bulk samples

Sixty-three quartz and fourteen carbonate samples were selected for crush leach analysis as described in Banks and Yardley (1992), Banks et al. (2000) and Gleeson (2003). Quartz samples were treated with HNO_3 in a sand bath to remove possible contaminations. 1- to 2-mm quartz and carbonate grains were cleaned by boiling and washing three times in milli-Q water. About 1 g dried sample was transferred to an agate mortar, 5 mL of milli-Q water was added and samples were crushed for 2 min for carbonate and 3 min for quartz. The solutions were filtered through 0.2- μm nylon filters prior to analysis. The leachates were analysed for F^- , Cl^- , Br^- , I^- , SO_4^{2-} by ion chromatography (Dionex DX-500) with a micro membrane suppressor. Cations (Li^+ , Na^+ , K^+ , Mg^{2+} , Ca^{2+}) were analysed in aliquots of the same solution by a Dionex DX-120 system.

4. Results

4.1. Petrography

All rocks were petrographically and mineralogically studied in polished thin sections. The samples have been subdivided into two major groups: metasedimentary and metavolcanic rocks. The list of samples and details petrographical observations from the Awak Mas and Salu Bullo are available in Appendix A.

4.1.1. Metasedimentary rock

The metasedimentary unit in the Awak Mas region includes phyllite, carbonaceous phyllite, chlorite-phengite schist and metasandstone-metasilstone, whereas metasedimentary rocks in Salu Bullo are dominated by hematitic mudstone and metasandstone-metasilstone.

Phyllite is composed of well-orientated quartz, white mica (phengite), siderite and albite (Fig. 3a). Augen, mottled and flaser textures are commonly observed. Rutile, apatite, zircon, monazite, xenotime and tourmaline occur as accessory minerals. Some of the apatite has a coarse grain size up to 1 mm in diameter; monazite and zircon are less than 40 μm and 80 μm , respectively. Sulphide and sulphosalt minerals are preserved either parallel to or cutting foliation.

Carbonaceous phyllite contains thin carbonaceous layers (less than 1 cm; Fig. 3b) and is commonly deformed with notable angular lithic clasts of quartz, chlorite and calcite (Fig. 3g). The constituent minerals are graphite, quartz, albite, phengitic mica, with small amounts of siderite, apatite and opaque minerals with framboidal along the foliation planes. Carbonaceous phyllite may contain gold, galena, mercurian tetrahedrite, sphalerite. Deformed carbonaceous phyllite is altered by chlorite.

Chlorite-phengite schist is a highly deformed rock, composed of chlorite, phengitic mica, with porphyroclasts of quartz, Fe-chlorite (chamosite) and pyrite. The foliation is intense and phengite shows remarkable parallelism to foliation. In addition, the rock is segregated into chlorite-rich and phengite-rich domains parallel to schistosity.

Minor apatite, calcite and rutile are observed as accessory minerals. The abundance of chlorite and albite as well as the absence of quartz and muscovite may imply a protolith with a mafic composition. Opaque minerals are pyrite, chalcopyrite and galena.

Metamorphosed quartz sandstone (metasandstone to metasilstone) is a massive crystalline rock essentially composed of quartz. The mineral assemblage is quartz, albite and minor hematite, and the rock is commonly altered by carbonate and/or sericite.

Hematitic mudstone is a red to brown fine-grained rock (Fig. 3c) and the mineralogy comprises albite + quartz + calcite + rutile + apatite + monazite with abundant sulphide (pyrite, chalcopyrite, sphalerite), sulphosalt (tetrahedrite-tennantite), galena, sphalerite and gold. This lithology has high gold grades (i.e. 8.94 ppm Au). It may be inferred that the hematitic mudstone is a product of intensive hydrothermal alteration.

4.1.2. Metavolcanic rocks

The most striking host rocks difference between the Awak Mas and Salu Bullo is the presence of mafic metavolcanic rocks, which are restricted to the upper part of the sequence at Salu Bullo. These are clinopyroxene- or plagioclase-phyric metamafics, chlorite-actinolite schist or greenschist, metatuff and meta-andesite. Volcanoclastic materials are included in this description because most magmatic components (clinopyroxene, chromian spinel) are often still preserved.

Clinopyroxene- or plagioclase-phyric metamafics retain some relic igneous minerals and textures, including primary magmatic minerals such as pyroxene (augite), plagioclase, Fe-Ti oxide and chromium spinel. Primary clinopyroxene is commonly observed as coarse grains, sometimes up to 1 mm and is partially altered by chlorite or actinolite. Chromium spinel forms euhedral – subhedral grains with variable size ranging from < 10 μm up to 80 μm in diameter; they occur as inclusions in clinopyroxene phenocrysts or in silicate matrix (Hakim and Melcher, 2017a). Plagioclase is altered to pure albite, chlorite, epidote or sericite.

The greenschist (Fig. 3d) described in this study is a metamafic commonly composed of pumpellyite + epidote + actinolite + quartz + albite + sphene + calcite. Chromian spinel is highly deformed, anhedral, generally less than 50 μm in diameter and commonly surrounded by chlorite and pumpellyite.

Metatuffite is characterized by a variable concentration of components, including tuff and bioclastic materials. These rocks have greenish to gray colors and are fine-grained with veins filled by late-stage calcite, quartz or albite. Petrographic observations indicate that the volcanoclastic rocks are metamorphosed to greenschist facies. This rock contains well preserved relic clinopyroxene and chromian spinel that are replaced by chlorite, quartz, albite, with minor actinolite, sericite and clay minerals.

Meta-andesite is a medium greenish-gray fine grained rock in which no quartz can be seen macroscopically. Thin sections show that meta-andesite consists mainly of albite, minor quartz, calcite, siderite-ankerite (confirmed by SEM-EDS) and hematite. Albite is altered to sericite. The meta-andesite sometimes preserves augite relics and epidote, and can be best classified as basaltic meta-andesite.

4.2. Hydrothermal alteration and mineralization

All rocks from drill core are moderately to intensely hydrothermally altered, strongly influenced by the host rock composition. Silica, carbonate, white mica and albite alteration are distinguished. Sericitization is observed in mafic metavolcanic rocks. The proximal alteration is mainly albite and silica whereas most distal alteration is dominated by secondary chlorite, calcite and lacks hydrothermal sulphide minerals. Chlorite and dolomite-ankerite occur in the altered mafic host rocks (Fig. 4c).

Silicification is characterized by the replacement of initial minerals by quartz accompanied by the deposition of sulphides (mainly pyrite-chalcopyrite) and extends from the veins outward into the host rock.

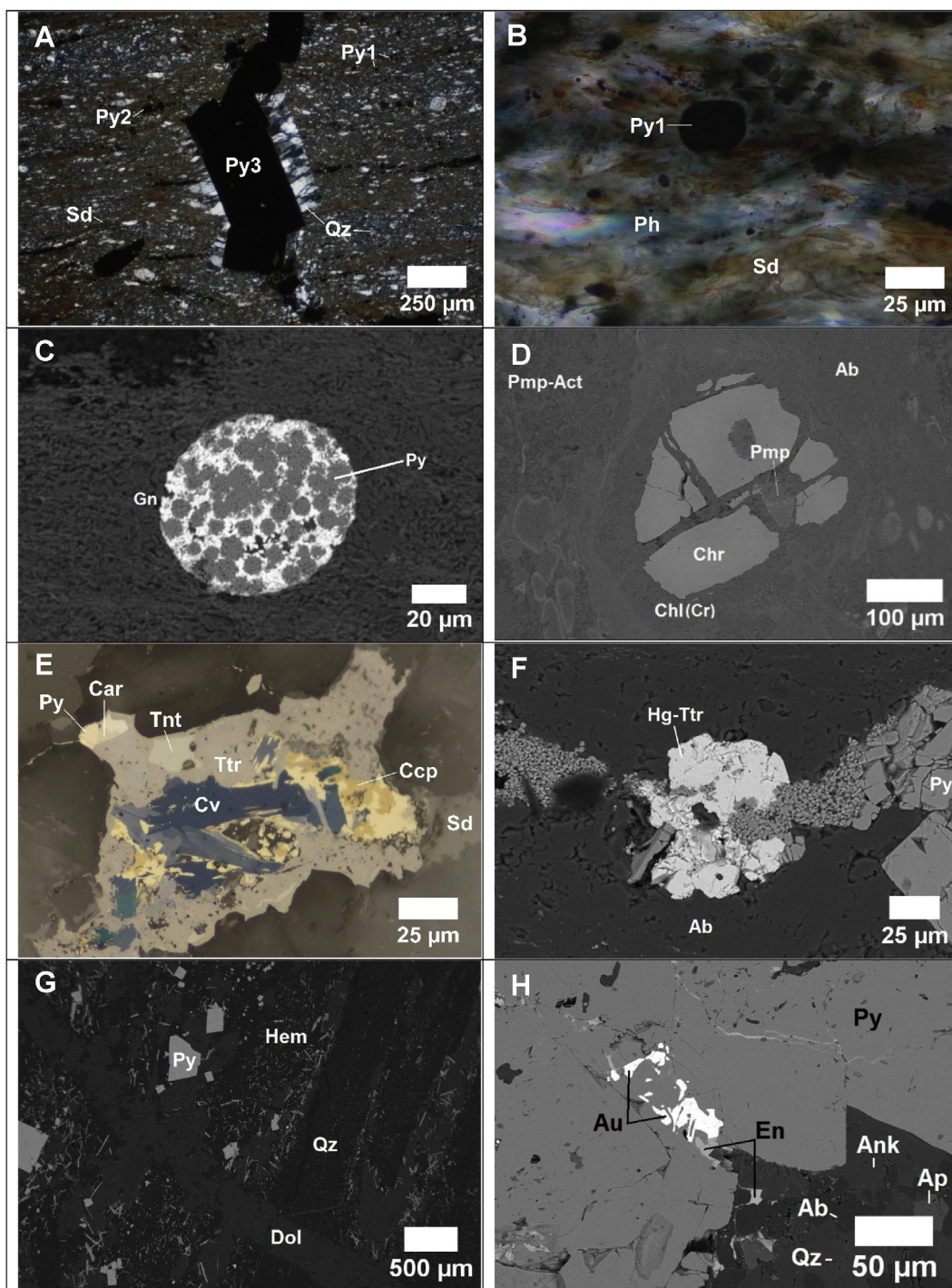


Fig. 4. Photomicrographs of borehole samples. (a) XPL image of three generations of pyrite observed in phyllite: framboidal pyrite (py_1) and euhedral pyrite (py_2) parallel to foliation; py_3 crosscutting foliation. (b) XPL image of framboidal pyrite in mica schist. (c) Electron back-scattered image of galena associated with framboidal pyrite. Silicate is albite. (d) Back-scattered image of chromian spinel grains surrounded by chlorite – pumpellyite – actinolite – albite. Chlorite contains up to 0.78 wt% Cr_2O_3 . (e) PPL image of complex sulphide \pm sulphosalt assemblage rimmed by siderite. (f) Back-scattered image of Hg-tetrahedrite containing up to 16.71 wt% Hg. (g) Veinlet of platy hematite host in phyllite. (h) Gold (bright phases) inclusions in pyrite. Abbreviations after Whitney, Evans (2010). Ab:albite, Act:actinolite; Au:electrum; Car:carrollite; Ccp:chalcocopyrite; Chl(Cr): chromian chlorite; Chr:chromian spinel; Cv:covellite; Dol:dolomite; En: enargite; Hem:hematite; Hg-Ttr: mercurian tetrahedrite; Ph:phengite; Py:pyrite; Sd:siderite; Tnt:tennantite; Ttr:tetrahedrite; Pmp:pumpellyite; Qz:quartz.

Minor siderite is also present as thin rims around sulphides (Fig. 4e). Albite alteration is observed in host rocks of all compositions (Fig. 4f). Argillic alteration (kaolinite) is less common.

The presence of oxide and sulphide – sulphosalt assemblages in addition to disseminated pyrite provides a diagnostic feature to distinguish three vein types in a chronological order as: (i) quartz – pyrite

Au veins, (ii) quartz – pyrite \pm sulphosalt Au veins, and (iii) barren veins.

Quartz – pyrite Au veins. The first type of gold mineralization is found in stockworks of pyrite with lesser amount of hematite (Fig. 4g); galena and sphalerite are minor sulphides with gold enclosed in coarse-grained (> 100 μm) pyrite. Based on crosscutting relations, quartz – pyrite Au

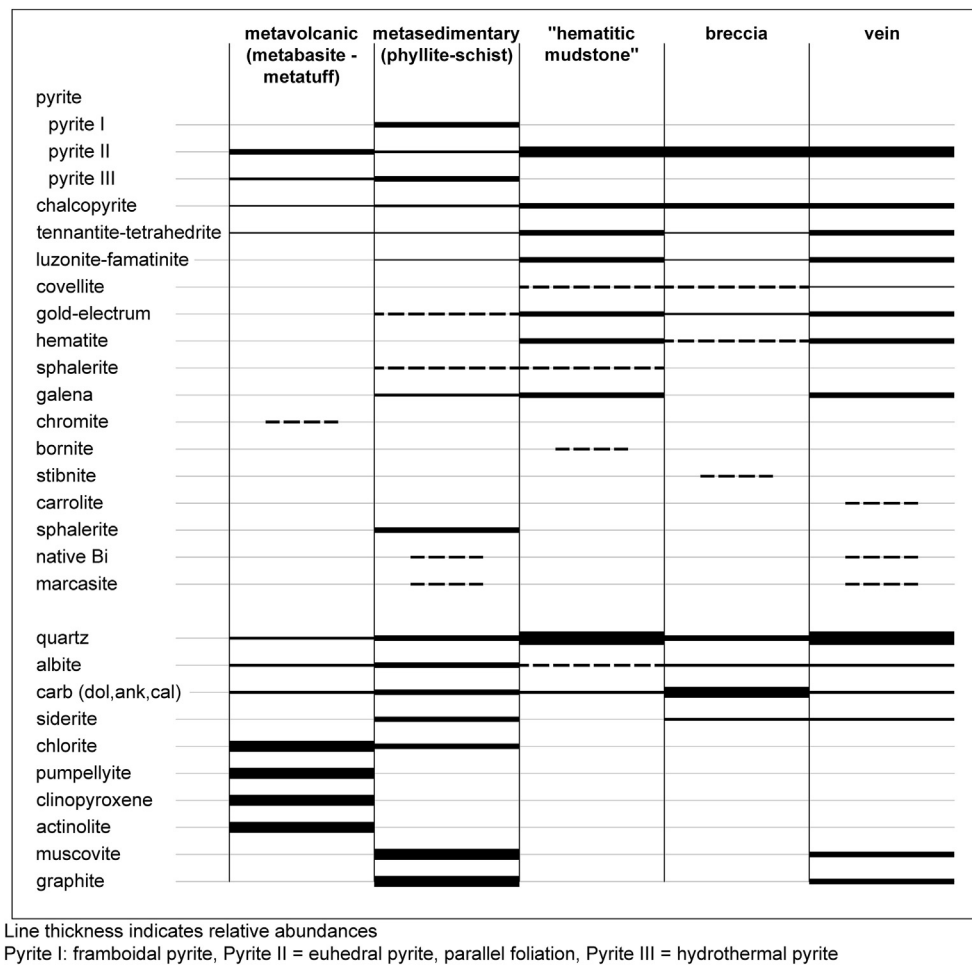


Fig. 5. Simplified paragenetic sequence of main ore and alteration minerals in the Awak Mas and Salu Bullo deposits.

veins are often cut by later generations of barren veins, (i.e. calcite – hematite veinlets). Hematite is tabular, disseminated, and homogeneous without any exsolution textures. Rutile and sphene occur commonly in this vein type, associated with a silica + albite alteration.

Quartz – sulphide (sulphosalt) Au veins. The second type of gold mineralization is characterized by disseminated pyrite with Cu-As-Sb-Zn-Fe-(Pb) minerals (i.e. chalcopyrite, tetrahedrite-tennantite, sphalerite). Almost all gold occurs as inclusions in pyrite with less free gold in quartz, and the grain size of gold ranging from 2 to 50 μm (average of 10 μm). This type of vein often hosts high gold grades (up to 10–15 g/t). Both vein types (quartz – pyrite Au veins and quartz – sulphide (sulphosalt) Au veins) are structurally controlled.

Barren veins. Barren veins consist of open-space fillings by quartz and/or albite + carbonate (mainly dolomite). Data indicate that these veins contain less than 0.5 ppm of Au and are of little economic interest. Barren veins are widespread in all mineralization stages.

Beside the ores described above, high-grade gold also occurs in the oxidation zone near the surface at Salu Bullo, in hematitic mudstone, breccia quartz-albite veins, and in thin quartz veins within the carbonaceous phyllite at Awak Mas. Processes of surficial oxidation have extensively altered iron sulphides, so that much of the gold was released from the sulphides. Supergene gold grade reaches up to 13 ppm in this zone with most gold occurring as a free gold, mainly in quartz. In carbonaceous phyllite at Awak Mas, sulphides commonly occur within graphite layers, with gold contents generally lower than 1 ppm. Sulphides mainly consist of pyrite, chalcopyrite, galena, tetrahedrite with minor sphalerite and rare native bismuth.

Three pyrite generations are observed. The first phase (Py1,

Fig. 4a–c) comprises finely disseminated grains of diagenetic, framboidal pyrite within gray to dark mica schist, phyllite or carbonaceous phyllite. The size of Py1 ranges from 10 to 50 μm , with some framboidal pyrite is partially replaced by galena (Fig. 4c). The second phase pyrite (Py2) shows euhedral to subhedral cubic shapes, ranging from 20 μm up to several hundred microns (Fig. 4a). This type of pyrite consists of pyrite bands that are coarse grained and parallel to bedding. The third phase (Py3) is a late hydrothermal pyrite that mainly occurs as large cubes up to millimeter size; it is idiomorphic, crosscutting bedding, or disseminated and associated with quartz veins (Fig. 4a). Hydrothermal pyrite (Py3) often over-grows earlier pyrite generations. The results of electron microprobe and in situ laser ablation-inductively coupled mass spectrometry in different types of pyrite provide evidence for trace element enrichment of Co, Ni, As with low Cu, Zn, Se, Bi, Au, and Ag (Hakim, 2017).

Chalcopyrite in the Awak Mas and Salu Bullo deposits occurs as different textural types: (i) as inclusions in pyrite, (ii) as free grains in silicates (quartz, albite, pumpellyite) or carbonates, or (iii) as randomly dispersed blebs in sphalerite (“chalcopyrite disease” of Barton Jr. and Bethke, 1987). Chalcopyrite is often replaced by tetrahedrite-tennantite and covellite (Fig. 4b). Bornite is a trace mineral (less than 5 μm in length) and is replaced by pyrite.

Chalcopyrite is found to have a strong correlation with sulphosalt minerals. Minor and trace sulphosalt minerals are tennantite, tetrahedrite, and enargite (Fig. 4h). They show a wide compositional variation, ranging between the As and Sb end-members. The disseminated, anhedral grains usually are intensely zoned due to Sb-As substitution. Based on electron-microprobe analyses of sulphosalts, tetrahedrite_{ss}

shows replacement of Cu by Hg, with some samples containing elevated Hg contents up to 17.28 wt% (Hakim and Melcher, 2016a) (Fig. 4f). Enargite/luzonite forming grains up to 100 µm in size is also notable in this vein type. The stoichiometry of enargite/luzonite calculated from the electron microprobe ranges from $Cu_{3.06}As_{0.93}Sb_{0.07}S_4$ to $Cu_{3.08}Sb_{0.84}As_{0.20}S_4$ (Hakim and Melcher, 2016a). Carrolite and covellite occur as trace minerals (Fig. 4e). Rare bismuthinite (3 µm in diameter) hosted by chalcopyrite and one grain of native bismuth (4 µm in diameter) surrounded by kaolinite are also reported from the studied samples (Appendix A). However, it is important to note that bismuth, bismuthinite and kaolinite are uncommon minerals in the Awak Mas District. The ore mineral paragenesis and mineral abundances are given in Fig. 5.

4.3. Electron microprobe analysis of chlorite and mica

The chlorite occurs as vesicle fillings or in veinlets, mostly in mafic host rock or chlorite schist. In the optical microscope, the chlorites have blue and green birefringence colours. In total, eighty-two electron microprobe analyses were obtained from seven samples. Chlorite from Salu Bullo has higher Mg-number [$100 \times Mg / (Mg + Fe^{tot}) = 43.6-73.6$] than at Awak Mas (Mg-number = 27–54.1) (Table 1a). Silica contents vary from 5.28 to 6.24 cations per 28 oxygens. The ternary diagram of the relative atomic proportions of Al, Fe, and Mg shows that chlorite from Salu Bullo falls into the clinocllore field, while chlorite in Awak Mas is classified as chamosite (Fig. 6a). Some samples (S53-50.20; greenschist and A687-157.90; chlorite schist) contain elevated amount of Cr_2O_3 (up to 0.78 wt%) and TiO_2 (average of 1.67 wt%, $n = 5$).

SEM and electron microprobe analyses show that much of the phyllite consists of fine-grained white mica interlayered with Ab + Qz + Sid ± Cc ± graphite. Twenty-four spot analyses of white mica were performed. The Si content in mica ranges between 3.2 and 3.51 per formula unit (average of 3.37 per formula unit) and Al between 1.91 and 2.58, indicating a strong phengitic substitution (Table 1b and Fig. 6b). The complete chlorite and mica datasets are given in the Electronic Appendix B.

4.4. Fluid inclusion petrography

Fluid inclusions in various assemblages occur in quartz, dolomite and plagioclase (albite). We focus on quartz and dolomite because most inclusions in albite occur as cloudy, irregular inclusions less than 5 µm in diameter, which may be regarded as secondary inclusions.

4.4.1. Fluid inclusions in quartz – pyrite Au veins

Pyrite ± hematite-Au quartz veins are represented by samples MP01.1, MP02 and MP03 (Table 2). Based on the compositional types

of fluid inclusion, three different types are distinguished: low salinity aqueous inclusions with CO_2 (type I), H_2O -NaCl (type II) and H_2O -NaCl containing solid phases (type III).

Quartz: inclusion type I. The inclusions contain liquid-vapour CO_2 or vapour CO_2 -liquid H_2O at room temperature with sizes between 5 and 15 µm (Fig. 7a–c). Inclusions occur isolated and scattered in quartz veins, which may imply a primary origin (Fig. 7a). H_2O with minor amounts of CO_2 are the main volatiles in the measured fluid inclusions (Fig. 8a–b). Quartz from the early-stage veins (sample MP02) is characterized by strong deformation textures and shows polygonal grains with grain boundaries meeting at 120-degree angles. Regular shaped inclusions are less common (Fig. 7b).

The volume fraction of vapour is about 0.14–0.15 with CO_2 with mole fraction less than 0.15 ($\chi^{vap} = 0.10$ to 0.144) (Table 2). Minor N_2 was detected in some of the inclusions with some low-ordered graphite (Fig. 8b).

Quartz: inclusion type II. Type II inclusions are one-phase (L_{H_2O}) or two-phase ($V_{H_2O} + L_{H_2O}$) liquid-rich aqueous inclusions (Fig. 7d and Fig. 8b). They generally have round (Fig. 7d), irregular (Fig. 7i) to elliptical shapes, ranging from 5 to 40 µm in diameter. These most abundant inclusions occur in clusters and sometimes as trails along healed fractures, which do not cut across the crystal boundaries of quartz. These features suggest a primary or pseudo-secondary origin.

Quartz: inclusion type III. These inclusions are one-phase inclusions with locally small opaque mineral inclusions that were identified as anatase (5 µm in size) using Raman spectroscopy (sample MP02). The inclusions contain about 10 vol% liquid phase at room temperature (Table 2).

4.4.2. Fluid inclusions in quartz – sulphide (sulphosalt) Au veins

Quartz: inclusion type-II. Observations for this type of inclusions are based on samples A685-5, A676-73.10 and A685-20. The inclusions are relatively large, 5 to 20 µm in diameter and have regular shapes. The volume fraction of vapour ranges from 0.12 to 0.21 (Table 2).

Quartz: inclusions type-III. Type III inclusions are one-phase (L_{H_2O}) inclusions with small trapped solid phases; they reach up to 12 µm (Fig. 7f) and have irregular shapes. The inclusions are randomly distributed in the quartz crystals. Solid phases were identified as quartz, calcite or tourmaline by Raman spectroscopy (Fig. 8d). These minerals may be regarded as accidentally trapped crystals.

4.4.3. Fluid inclusions in barren veins

Quartz: inclusion type II. Inclusions in sample GRS08 range from 5 to 20 µm in size and have regular to irregular elongated shapes. Sample A687-235 also contains barren veins. Volume fractions of FI from barren quartz veins in samples GRS08 and A687-235 are highly variable, ranging from 0.15 to 0.25 and from 0.10 to 0.38, respectively (Table 2). Fig. 7g illustrates type-II fluid inclusions in quartz with

Table 1a

Chemical parameters (mean and range) of Mg-rich chlorite in the Salu Bullo and Fe-rich chlorite in the Awak Mas.

Salu Bullo	S66-122.50	S68-84.55	S68-69	S68-47	S53-50.20	S68-39.10	S68-34.90
Number of analyses	6	2	10	12	13	15	10
Elevation (m)	948.26	971.14	984.48	1002.5	1005.88	1008.97	1012.41
Depth (m)	106.90	118.53	56.52	38.50	41.12	32.03	28.59
wt% TiO_2	0.02 (0–0.08)	0.16 (0–0.3)	0.02 (0–0.06)	0.01 (0–0.05)	0.02 (0–0.06)	0.01 (0–0.03)	0–0.04
Mg-number	49.5 (43.4–53.3)	55.4 (54.6–56.1)	66.2 (61.9–71.8)	72.2 (70–73.6)	72.1 (71.1–72.9)	69 (66–72.2)	71.6 (69.3–73.1)
T (°C)	308 (296–325)	300 (291–308)	272 (252–289)	257 (234–280)	260 (236–276)	253 (227–272)	260 (243–276)
Awak Mas		A685-171		A687-157.90			A192-155.70
Number of analyses		4		5			5
Elevation (m)		1033.91		1043.25			1059.51
Depth (m)		148.09		136.75			135.19
wt% TiO_2		0.48 (0.09–1.10)		1.67 (0.01–5.47)			0.38 (0–1.36)
Mg-number		31.6 (27–32)		47.4 (45.5–52.9)			37.3 (34.1–39)
T (°C)		372 (362–376)		321 (269–346)			359 (347–373)

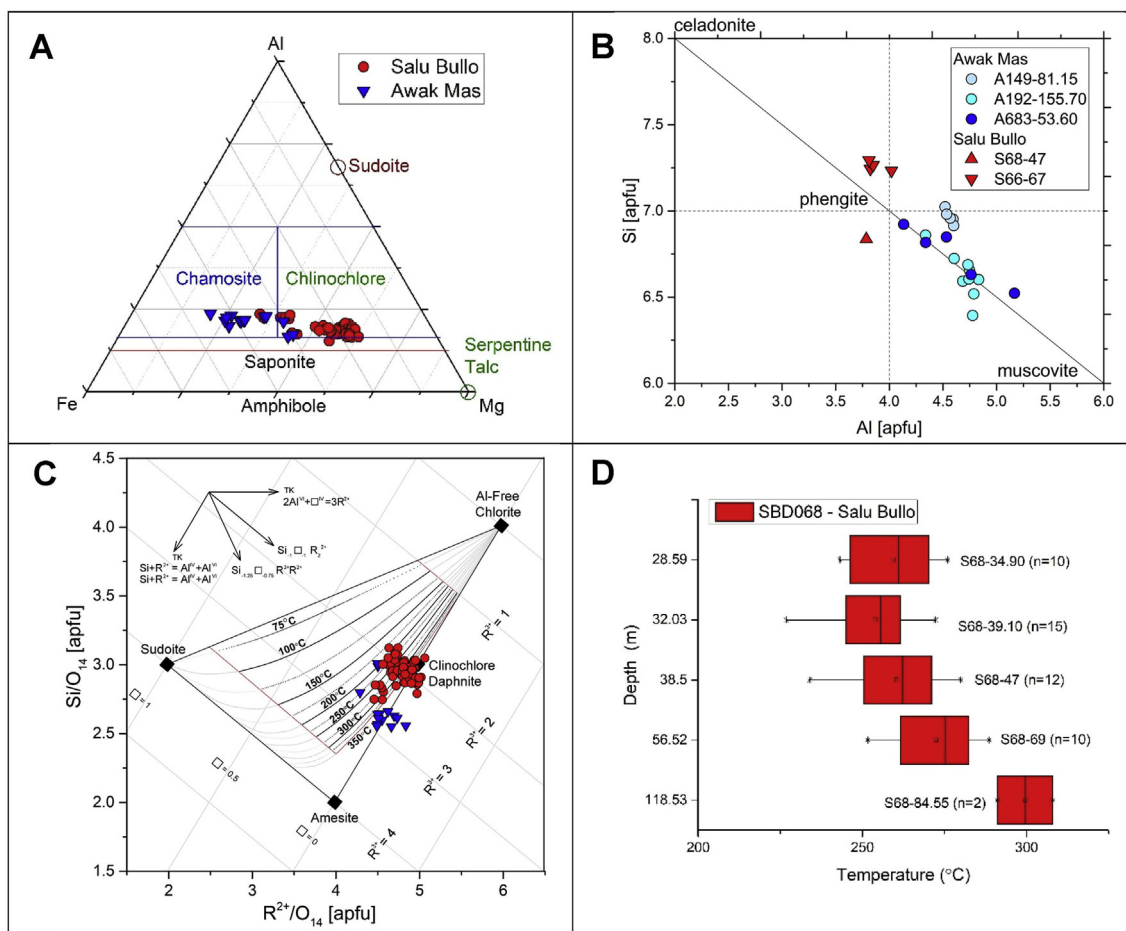


Fig. 6. Composition of chlorite and mica obtained by electron microprobe analyses. (a) Ternary diagram of chlorite. (b) Classification of representative white mica phases in the diagram Si vs. Al. (c) Graphical chlorite geothermometer after Bourdelle and Cathelineau (2015). (d) Chlorite geothermometer based on Kranidiotis and MacLean (1987) for bore hole SBD068.

variable volume fractions.

Dolomite: inclusion type II. Fluid inclusions in dolomite are regular shaped inclusions between 5 and 10 μm in diameter (Fig. 7e). Sample A687-235-dol contains two-phase (V_{H2O} + L_{H2O}) liquid-rich aqueous inclusions (type II), with a highly variable volume area fraction between 0.12 and 0.46 (Fig. 7h).

4.5. Microthermometry

4.5.1. Fluid inclusion in quartz – pyrite Au veins

The melting temperature of solid CO₂ in type I inclusions [T_m

(CO₂)] ranges between –57.5 and –56.6 °C (Fig. 9a, see Electronic Appendix D). This is close to the triple point of pure CO₂ (–56.6 °C) and indicates that the gas phase is mainly composed of CO₂ with some contribution of N₂ (Fig. 8b). Clathrate completely dissolves (T_m clathrate) at temperatures between 8.6 and 9.9 °C (Fig. 8b) with the presence of liquid and vapour CO₂. Homogenization temperatures of aqueous-carbonic CO₂ [Th (CO₂)] ranges from 25.4 to 31 °C (Fig. 8c).

The final dissolution of ice (T_m ice) occurs in a narrow temperature range between –3.6 and –2.8 °C (Fig. 8b). Liquid and vapour phases homogenize from 146.3 to 177.5 °C (Fig. 9a). Densities of the bulk type I inclusions are relatively homogenous, between 0.96 and 0.99 g/cm³

Table 1b

Chemical parameters (mean and range) of Mg-rich mica in the Salu Bullo and Awak Mas deposits.

	S68-47	A192-155.70	A683-53.60	A149-81.15
Number of analyses	1	9	5	5
Elevation (m)	1002.5	1059.1	1079.91	1119.87
K/(K + Ca + Na)	0.99	0.97 (0.95–0.98)	0.97 (0.94–0.99)	0.96 (0.95–0.98)
wt% K ₂ O	10.49	9.99 (8.39–10.95)	9.44 (7.36–10.93)	9.30 (9.09–9.62)
Si (a.p.f.u)	6.84	6.63 (6.39–6.86)	6.75 (6.52–6.92)	6.97 (6.91–7.02)
Al (a.p.f.u)	3.79	4.69 (4.34–4.83)	4.59 (4.13–5.17)	4.56 (4.52–4.60)
Mg-number	70.8	56.1 (42.7–65.7)	59.5 (49.3–66.1)	98.8 (97.5–99.9)
Pressure (kbar) [*]	8.2 (7.8–8.5)	7.3 (4.2–9.7)	7.9 (4.6–11.1)	11.1 (10.4–13.1)
Temperature (°C)	257 (234–280) ¹	360 (327–377) ²	395 (361–405) ²	372 (339–393) ³

* Calculated using phengite barometry of Massonne and Schreyer (1987).

¹ Chlorite geothermometry from the same sample (this study).

² Graphite thermometry from the same sample (this study).

³ Graphite thermometry of phyllite from the sample A192-155.50 (this study).

Table 2
Summary of microthermometric data for fluid inclusions at gold deposits within Latimojong.

Sample	n	Volume fraction (vap)	Inclusion type	Size (μm)	Bulk density (g/cc)	$T_m(\text{CO}_2)$ ($^{\circ}\text{C}$)	$T_m(\text{ice})$ ($^{\circ}\text{C}$)	$T_m(\text{clath})$ ($^{\circ}\text{C}$)	$T_h(\text{total})$ ($^{\circ}\text{C}$)	Salinity (eq% NaCl)
Barren quartz veins										
GRS08	29	0.15–0.25	II	5 to 20	0.78 to 0.87		–3.80 to –1.60		180.60 to 284.00	2.74 to 6.16
A687-235	22	0.10–0.39	II	10 to 40	0.63 to 0.94		–2.40 to –1.30		165.60 to 344.70	2.24 to 4.03
Barren dolomite										
A687-235dol	21	0.12–0.46	II	5 to 10	0.55 to 0.89		–2.50 to –1.60		191.30 to 386.90	2.74 to 4.18
Quartz pyrite-Au veins										
MP01.1	25	0.10–0.13	II	5 to 10	0.92 to 0.93		–3.30 to –2.90		164.60 to 194.70	4.80 to 5.41
MP02	14	0.10–0.15	II,III	10 to 20	0.89 to 0.94		–3.80 to –2.70		157.70 to 211.30	4.49 to 6.16
MP02	5	0.14–0.15	I	3 to 8	0.85 to 0.99	–57.50 to –56.60	–3.60 to –2.80	8.60 to 9.90	146.30 to 177.50	4.70 to 5.94
MP3	46	0.10–0.18	II	10 to 40	0.87 to 0.93		–5.20 to –0.80		157.80 to 241.70	1.40 to 8.14
Quartz sulphide (sulphosalt)-Au veins										
A685-5	48	0.12–0.19	II, III	10 to 20	0.86 to 0.92		–3.60 to –2.40		184.60 to 243.20	4.02 to 5.86
A676-7310	26	0.13–0.15	II	10 to 20	0.88 to 0.89		–3.20 to –1.20		158.40 to 212.30	2.07 to 5.26
A685-20	18	0.15–0.21	II	5 to 10	0.83 to 0.90		–3.20 to –1.60		175.40 to 257.00	2.73 to 5.26

Inclusion type-I: $\text{H}_2\text{O}(\text{CO}_2)\text{-NaCl}$, type-II: $\text{H}_2\text{O-NaCl}$; type-III: $\text{H}_2\text{O} + \text{NaCl}$ with solid daughter minerals.

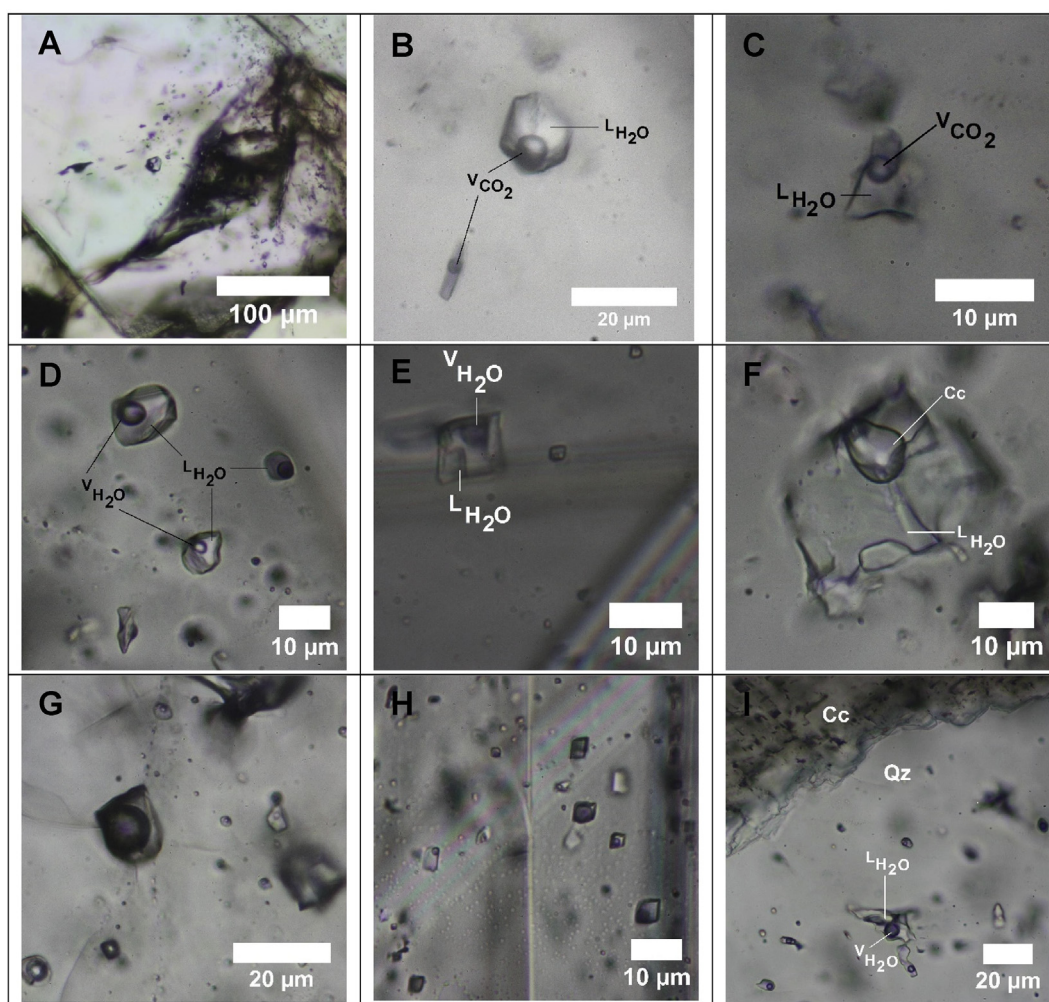


Fig. 7. Photomicrographs of fluid inclusions trapped in quartz at room temperature. (a) Isolated CO_2 bearing fluid inclusion hosted in quartz. (b). Enlargement of Figure 85A. A big isolated fluid inclusion containing liquid H_2O and vapour CO_2 at room temperature. Sample S69-25. (c) Type I inclusion hosted in quartz from sample MP02. (d) Primary aqueous inclusion of type II hosted in quartz grain from sample MP03. (e) Photomicrograph of type-II inclusions hosted in dolomite (A683-4680) (f) highly irregular shaped inclusion with calcite daughter crystal (inclusion type-III). (g-h) Photomicrograph of fluid inclusion type-II from sample A687-235 with variable volume fractions of the vapour phase hosted in quartz (g) and dolomite (h). (i) Irregular aqueous inclusions host in quartz.

(Table 2), with calculated salinities ranging from 4.70 to 5.94 eq. mass % NaCl (Table 2, Fig. 11).

During quantification of CO_2 inclusions, several difficulties were

encountered. The CO_2 bearing FIs are irregular (Fig. 7c) and most of the inclusions are less than $5\ \mu\text{m}$ in size. Only sample S69-25 contains regular shaped fluid inclusions (Fig. 7b). Gaseous species could be

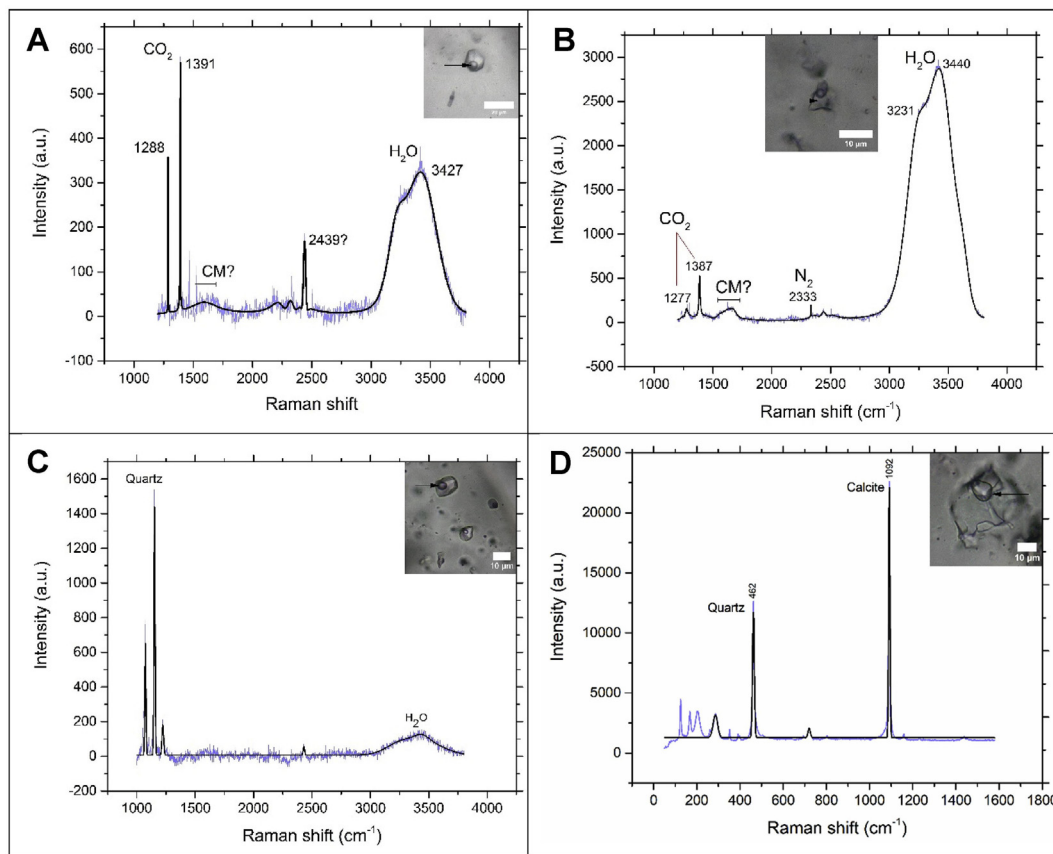


Fig. 8. Raman spectra of fluid inclusions. (a) CO₂-rich inclusion of type-I. (b) Aqueous inclusions with minor amounts of salt and CO₂ (type I). Inclusion probably contains trace amounts of CM (carbonaceous material) and N₂. (c) Type II fluid inclusion containing aqueous fluid. (d) Type III fluid inclusion with calcite as a daughter mineral. Blue and black lines indicate raw and processed spectra, respectively. (For interpretation of the references to colour in this figure legend, the reader is referred to the web version of this article.)

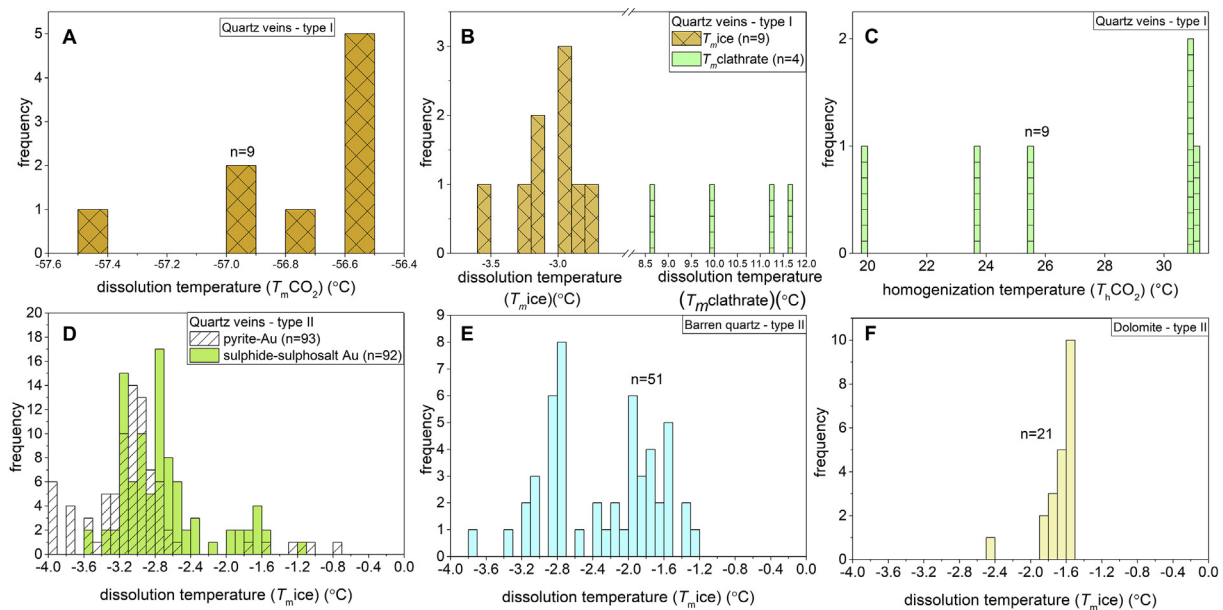


Fig. 9. Histogram showing the microthermometric results. (A) dissolution temperature of CO₂ from fluid inclusion type-I; (B) dissolution temperature of clathrate indicating low-concentration of CO_{2(V)} in the system; (C) homogenization temperature of CO₂; (D) dissolution temperature of type I and type II quartz-pyrite-Au veins; (E) dissolution temperature of barren quartz veins; and (F) dissolution temperature of barren dolomite veins.

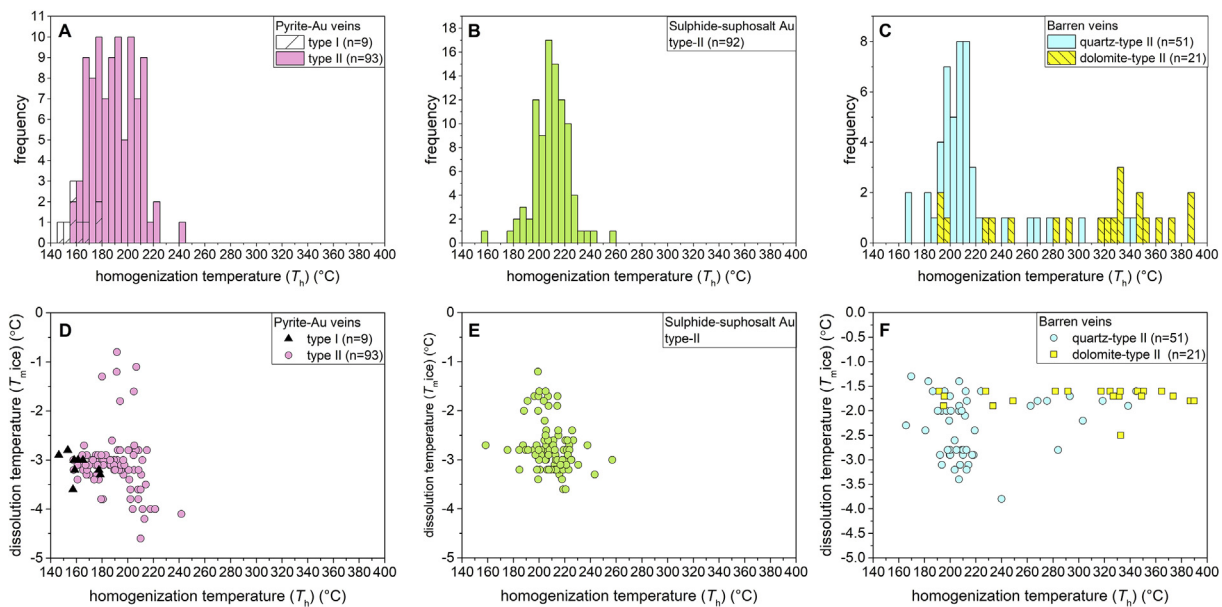


Fig. 10. Histogram showing the homogenization temperature from microthermometric observation of (A) type-I and type-II inclusion hosted in quartz-pyrite-Au veins; (B) sulphide-sulphosalt Au veins; (C) barren quartz-dolomite veins. Scatter plot of homogenization temperature versus dissolution temperature of (D) quartz-pyrite-Au veins. (E) sulphide-sulphosalt veins and (F) barren quartz-dolomite veins.

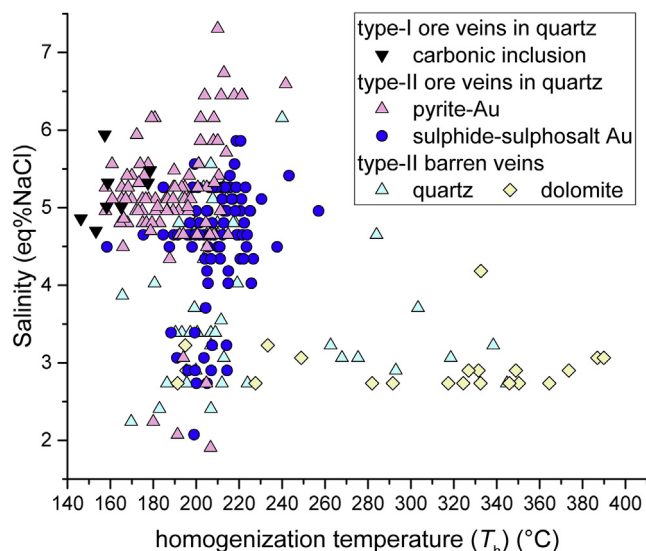


Fig. 11. Scatter plot of homogenization temperature versus salinity of mineralized and barren veins.

assessed using laser Raman spectroscopy (Fig. 8a-b) but observation and quantification using the heating freezing stage remains problematic. The FI are likely of type-I; results are shown in Fig. 9a-c and Fig. 10a.

Quartz: inclusion type II. The final dissolution temperatures of type II aqueous inclusions are bimodally distributed: (i) from -4.0 to -2.5 °C and (ii) from -1.8 to -0.8 °C (Fig. 9d). This data corresponds to a wide range of salinities between 1.4 and 7.3 eq. mass% NaCl (Fig. 11). The temperature of homogenization to the liquid phase is between 157.7 and 241.7 °C (Fig. 10a). Densities of the bulk inclusions range from 0.85 to 0.94 g/cm³ (Table 2).

4.5.2. Fluid inclusion in quartz – sulphide (sulphosalt) Au veins

Quartz: inclusion type II. The final dissolution temperature of ice in sulphide ± sulphosalt-Au quartz veins has a bimodal distribution with (i) ranging from -3.6 to -2.4 °C, and (ii) from -2.4 to -1.2 °C at an

average value of -2.76 °C (s.d. ± 0.78 , mode at -2.8 , see Fig. 9d), which produces calculated salinities between 2.1 and 5.9 eq. mass% NaCl (Fig. 11). The bulk density is between 0.83 and 0.92 g/cm³ (Table 2) and the total homogenization is between 158.4 and 243.2 °C, with a mode at 207.4 °C (Fig. 10b).

4.5.3. Fluid inclusion in barren veins

Quartz: inclusion-type II. Final ice dissolution temperatures are at a mode of -2.8 °C (ranging from -3.8 to -1.3 °C, Fig. 9e), corresponding to salinities ranging from 2.24 to 6.16 eq. mass% NaCl equivalent (Fig. 11). Total homogenization of vapour phases occurs from 165.60 to 344.70 °C (Fig. 10c). The bulk density of FI in sample 687–235 is highly variable, between 0.63 and 0.94 g/cm³ (Table 2).

Dolomite: inclusion type II. Type II inclusions hosted in dolomite yield final melting temperatures from -2.5 to -1.6 °C (Fig. 9f), corresponding to salinities between 2.74 and 4.18 eq. mass% NaCl equivalent (Table 2). The total homogenization temperatures of FI in dolomite are highly variable, between 191.3 and 386.9 °C, with an average of 304.3 °C (Fig. 10c). These conditions define the maximum homogenization temperatures in this study. Densities of the bulk inclusions in dolomite range from 0.55 to 0.89 g/cm³ (Table 2).

4.6. Crush-leach analyses

The chemical composition of fluids extracted from quartz and carbonate from the drill core samples is summarized in Electronic Appendix E. The ratios of (I/Cl) versus (Br/Cl) discriminate the results into two groups based on lithology (Fig. 12a). Quartz yields log (I/Cl) averaging to -3.59 ± 0.31 (ranging from -4.48 to -3.26), whereas the average composition of barren carbonate is -3.36 ± 0.40 (ranging from -4.50 to -3.01) (Fig. 12a). The ratios of (Na/Cl) versus (Cl/Br) (Fig. 12b) from veins are distributed into two groups: (i) Na/Cl molar ratios < 1.8 with Cl/Br ratio ranging from 1068 to 5433; and (ii) Na/Cl molar ratios > 1.8 with Cl/Br ratio ranging between 734 and 2874. Furthermore, materials barren with respect to gold are characterized by Na/Cl and Cl/Br molar ratios > 0.68 and < 3065 , respectively (Fig. 12b and Electronic Appendix E).

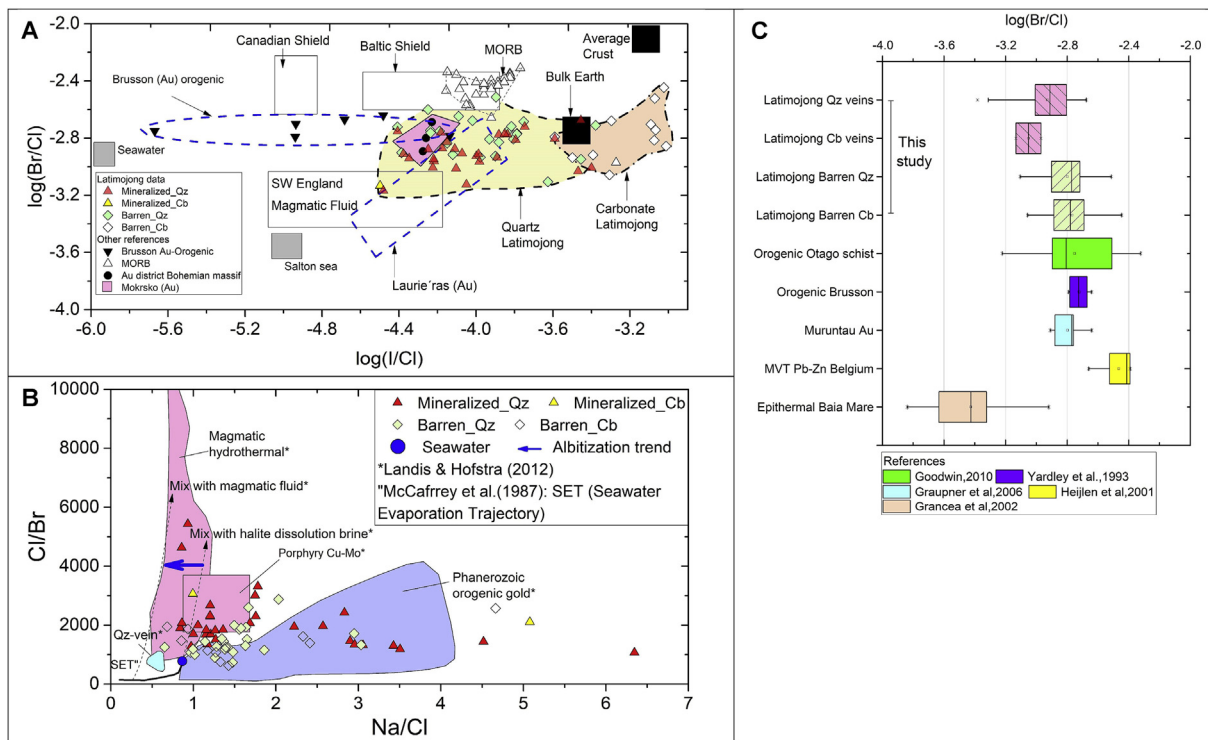


Fig. 12. Halogen data for quartz and carbonate. (A) Log (I/Cl) vs. log (Br/Cl) mole ratios for crush leach analyses obtained on gold bearing quartz-carbonate veins from the Latimojong metamorphic complex. Literature data for other crustal fluids: Frape, Fritz, 1987; Yardley, 1993; Boiron et al., 2001, 2003; Kendrick et al., 2012. (B) Molar Na/Cl vs. Cl/Br plot of fluid inclusion extracts from quartz and carbonate (Landis, Hofstra 2012). The black line shows the evaporation path along the seawater evaporation trend (SET). (C) The Br/Cl molar ratios of veins in the Latimojong Metamorphic Complex compared to literature data.

4.7. Raman spectroscopy on carbonaceous materials

The extracted spectral parameters (Fig. 12 and Appendix C) are the Gmax (graphite band) and Dmax (defect band) band positions and STA (scaled total area, Lünsdorf and Lünsdorf, 2016). The Dmax and Gmax bands are the highest pseudo-Voigt values in the D- and G-band region, respectively. In addition, D_STA and G_STA represent the parameter the sum of the scaled sum-curve values of the Raman shift interval from 1000 to 1800 cm⁻¹ (Lünsdorf et al., 2017). The D1 band is observed between 1344 and 1354 cm⁻¹, whereas the G band occurs between 1580 and 1600 cm⁻¹ (Fig. 12a and b; Appendix C). Peak fitting demonstrates the presence of the D2 band at ca. 1,60 cm⁻¹ (Fig. 12a).

5. Geothermometry

5.1. Chlorite geothermometer

The chlorite geothermometer of Kranidiotis and MacLean (1987), which is based on the calculated Al^(IV) and corrected Fe/(Fe + Mg) ratio, indicate an average temperature of 268 °C (ranging from 227 to 372 °C, n = 82) (Table 1a). A similar result is obtained using the chlorite geothermometer of Bourdelle and Cathelineau (2015). A plot of T-R²⁺-Si (R²⁺ refer to divalent cations Fe²⁺ and Mg²⁺) diagrams indicates temperatures ranging from 200 to 350 °C (Fig. 6c).

The high amount of chromium in chlorite (i.e. S53-50.20 and S50-39.10, up to 0.8 wt% Cr₂O₃, Appendix B) correlates well with the presence of altered chromian spinel as an accessory mineral in mafic rock; thus, Cr may be interpreted as a mobile element during metamorphism. Sample A687-157.90 contains abundant titanium in chlorite (average of 1.7 wt% TiO₂, n = 5, Appendix B). This sample is characterized by an abundance of Ti-bearing minerals, including sphene and rutile, contributing to the high concentration of titanium in chlorite. Consequently, the high content of titanium in this chlorite will decrease the Al₂O₃ content due to the cation occupancy. As a result, the chlorite

geothermometer of Kranidiotis and MacLean (1987) in that sample gives a wide range of temperatures (from 269 to 346 °C, Table 1a).

Titanium-bearing chlorite has been reported from various localities in subgreenschist and lower greenschist facies rocks (Abdullah Atherton, 1964 in Force, 1991). Force (1991) suggests that the predominant titanium carrier in subgreenschist- and lower greenschist-facies rocks is mostly sphene, in upper greenschist-facies rock biotite and in the lower amphibolite facies hornblende (in mafic rocks) and sphene (all lithologies).

5.2. Cation geothermometer

Different geothermometers using cations in fluid leachates were applied. These are the Na-K geothermometer of Giggenbach (1988); the Na-K, Na-Li and Mg-Li geothermometer of Kharaka and Mariner (1989)

Table 3
Various geothermometers based on cation data.

		Na-K ¹ °C	Na-K ² °C	Na-Li ¹ °C	Mg-Li ¹ °C
Calcite (n = 3)	min	219.4	217.0	178.6	56.5
	max	257.3	248.5	233.3	98.4
	average	232.7	228.0	207.3	72.7
	S.D.	21.4	17.8	27.4	22.5
Dolomite-Ankerite (n = 13)	min	92.4	105.8	77.4	29.8
	max	454.7	401.2	248.5	136.6
	average	258.2	247.4	156.1	82.0
	S.D.	89.1	72.9	57.7	26.0
Quartz (n = 46)	min	148.6	156.2	102.8	50.1
	max	430.0	383.0	236.2	133.7
	average	294.5	277.5	164.6	93.6
	S.D.	69.1	55.9	30.9	22.9

¹ Kharaka and Mariner (1989).

² Giggenbach (1988).

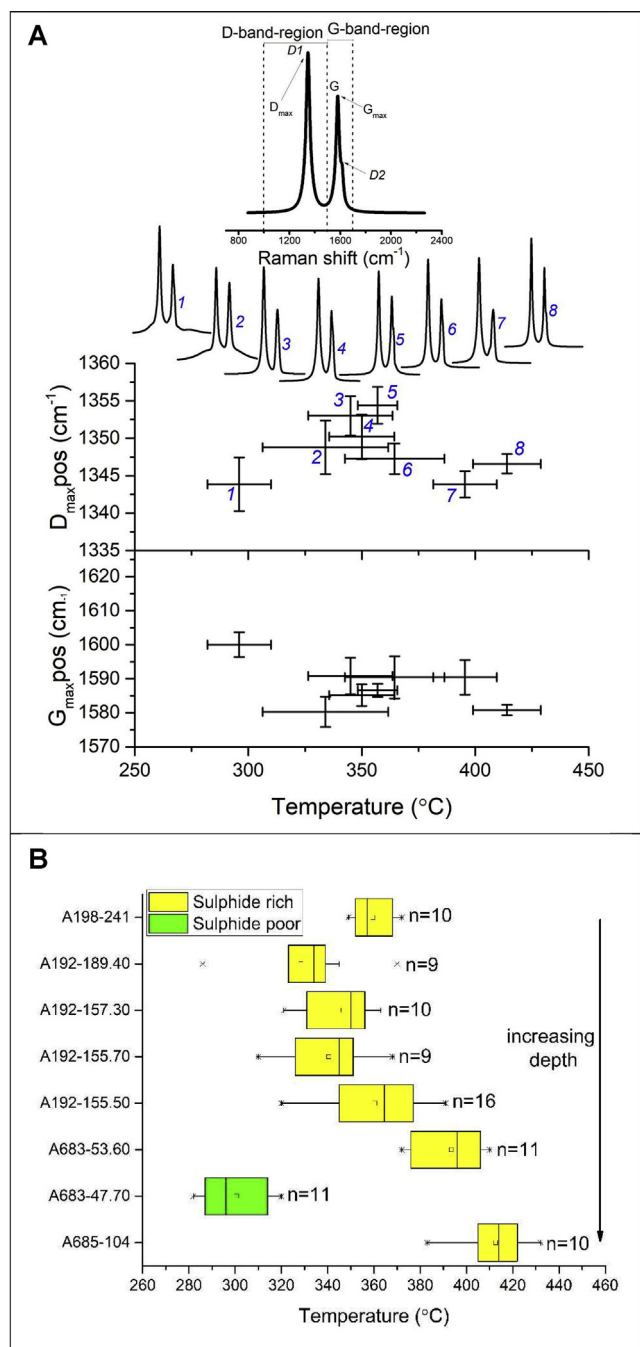


Fig. 13. Nomenclature of CM Raman Spectra and compilation of the most indicative Raman parameters obtained on the samples from the Latimojong. (A) Output of IFORS software (Lünsdorf and Lünsdorf, 2016). (b) Summary of formation temperature data of carbonaceous phyllite and carbonaceous breccia.

(Table 3 and Appendix E). The Na-K geothermometer yields highly variable results; the Na-K of Kharaka and Mariner (1989) yields 220–257 °C for calcite, 92–450 °C for dolomite-ankerite and 150–430 °C for quartz. Some samples have been excluded from calculations because they give unrealistic calculated temperature (i.e. the foraminifera sample has 1400 ppb K, 1100 ppb Na and 1.2 ppb Li, which gives Na-K temperature of > 600 °C, by contrast, Na-Li and Mg-Li geothermometer give low temperature of 150 °C and 40 °C, respectively). The results show that the Na-K and Na-Li geothermometers yield higher temperature than the Mg-Li geothermometer.

Petrographical observations show that dolomite-ankerite and siderite are associated with ore minerals (gold, sulphide and sulphosalt),

and therefore yield higher temperature than barren calcite which commonly occurs as crack- or vesicle-filling, and crosscutting mineralized veins. The calculated temperatures (Na-K, Na-Li) are comparable to the microthermometric results (see Section 4.5). Calculated temperatures above 400 °C may be interpreted as a metamorphic temperature of the greenschist-facies in the Latimojong Metamorphic Complex.

5.3. Formation temperature based on carbonaceous materials

The transformation of carbonaceous material to graphite is monitored by Raman spectra on carbonaceous materials (RSCM) in response to rising metamorphic conditions. With increasing structural order, the G and D₂ peaks are clearly distinguishable. The D₂ band appears on the side of the G band (Fig. 13a), similar to the spectra of semi-graphite of lower greenschist-facies metamorphic samples (Rantitsch et al., 2016), and also a blueschist-facies metamorphic sample from the Schistes Lustrés in the Western Alps (Beysac et al., 2002). With increasing metamorphic rank, both, the D₁ and the D₂ intensities decrease, whereas the G band increases (Fig. 13a, Appendix C; Lünsdorf and Lünsdorf, 2016). The results indicate that the carbonaceous phyllite of the Latimojong Metamorphic Complex is composed of poorly ordered carbonaceous material. Formation temperature calculations using the approach of Lünsdorf et al. (2017) suggest metamorphic temperatures between 296 and 414 °C (± 25 °C) (n = 86, Fig. 13b and Appendix C). Samples containing ore minerals yield higher temperature compared to barren samples (Fig. 13b).

6. Discussion

In the discussion, the question as to what degree the rocks have experienced metamorphism will be approached first. Fluid trapping conditions, pressure estimation and depth of formation will be calculated from the properties of fluid inclusion. Halogen data obtained from crush leach analysis are used to model the source of mineralizing fluids. The characteristics of the Awak Mas District will be presented in the ore deposit section. Finally, a genetic model of the Awak Mas District in relation to metamorphism and magmatism is proposed.

6.1. Pressure-temperature estimates

Phengite barometry (Massonne and Schreyer, 1987) and chlorite geothermometry (Bourdelle and Cathelineau, 2015; Kranidiotis and MacLean, 1987) in combination with temperature estimation on carbonaceous materials (Lünsdorf, 2015) are used to establish a possible *P-T* path, assuming that coarse white mica and semi-graphite reflect the maximum *P-T* conditions in the Awak Mas District. Isochores obtained from fluid inclusions illustrate the timing of mineralization related to metamorphism. It is important to mention that petrographic observations indicate that white mica from the studied samples is not always equilibrated with the rest of the minerals of the rocks. For example, the mineral assemblages are Ph + Qz + Ab + Gr in carbonaceous phyllite and Chl + Pmp – Ph with augite relics in greenschist. As noted by Massonne and Schreyer (1987), equilibrium problems of white mica in nature are commonly observed. These authors indicated that homogenization and re-equilibration of phengitic mica is an extremely sluggish process within geologic times scales; therefore, white mica still could be the key to unraveling the earlier stages of the metamorphic rock.

White mica in carbonaceous phyllites with Si contents of 3.19–3.48 a.p.f.u. (average of 3.37 a.p.f.u.) yields a huge pressure range of ca. 3.45–12.3 kbar (average of 7.9 kbar, Table 1b and Fig. 14a) (Massonne and Schreyer, 1987) at an estimated temperature of 300–415 °C (graphite geothermometer, Section 5.3). These values may represent the subduction between the Indo-Australian and Eurasian plates during the Late Cretaceous. Elevated pressure signatures are also recorded by the

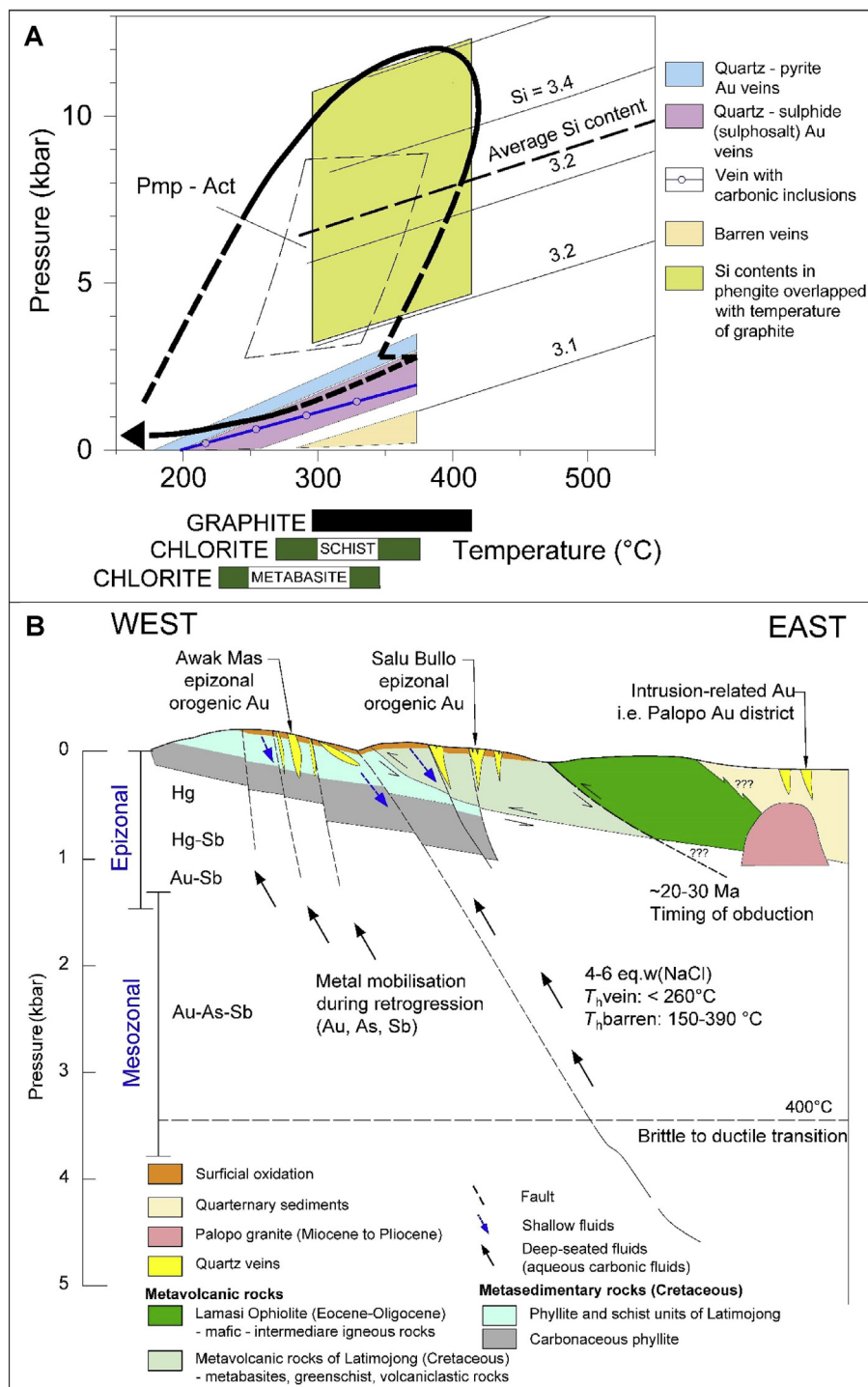


Fig. 14. (a) General *P-T* reconstruction of the conditions prevailing in the Latimojong Metamorphic Complex using the phengite barometer diagram from Massonne and Schreyer (1987), graphite geothermometry based on IFORS software (Lünsdorf and Lünsdorf, 2016), chlorite geothermometry according to Kranidiotis and MacLean (1987). The stability field of pumpellyite-actinolite is based on Liou et al. (1987). (b) Mechanism of structurally-controlled ore precipitation in the Latimojong metamorphic complex during retrograde metamorphism.

mineral assemblage of some greenschist samples (Pmp + Act + Epi). The latter mineral assemblage is important in petrogenetic studies in this region, since it represents key minerals of the blueschist-facies and likely the metamorphic peak in the Latimojong Metamorphic Complex. This will be discussed below.

In a low-grade metamorphic terrain, rocks containing albite + quartz may have, in addition, chlorite + pumpellyite in more ferroan compositions, chlorite + actinolite in magnesian bulk compositions, and prehnite in a low aluminium and ferric iron bulk rock

composition (Beiersdorfsser and Day, 1995). The first appearance of calcic amphibole as overgrowth on relict clinopyroxene and as acicular crystals in quartz marks the beginning of the Pmp + Act + Epi facies. The minerals prehnite, laumontite, lawsonite, and glaucophane are absent in the studied samples. The absence of these minerals provides important information, because they bound the stability field of Pmp + Epi + Act (Fig. 14a). Prehnite and laumontite are restricted to low pressures, whereas lawsonite and glaucophane are restricted to high pressures. With increasing temperature, the disappearance of

pumpellyite and prehnite and the appearance of albite – chlorite – actinolite – epidote – sphene mark the transition to greenschist facies assemblages. According to the stability field of Pmp + Epi + Act suggested by Beiersdorfsner and Day (1995), and the absence of prehnite, laumontite, lawsonite and glaucophane correspond to a wide pressure range, from 4 to 9 kbar at temperature between 200 and 350 °C.

6.2. Fluid trapping conditions

Most of the fluid inclusion assemblages described in this study are H₂O–NaCl fluids in type-II inclusions. Type-I inclusions were specified only in sample MP02 and are intersected by a later vein generation and fluid inclusions type-II. Quartz forms polygonal grains showing 120 degree angles indicating dynamic recrystallization in quartz at elevated temperature (Pettijohn et al., 1987). The presence of minor N₂ contributes to the melting of CO₂ below its melting point.

In order to illustrate the fluid evolution, a plot of total homogenization versus dissolution temperature has been constructed (Fig. 10d–f). Some aqueous-carbonic inclusions represent the minimum homogenization temperatures observed in this study (146–177 °C) (Fig. 10d), whereas dolomite yields the maximum homogenization temperature of 387 °C (Fig. 10f). Homogenization temperatures of quartz-pyrite-Au veins yield maximum temperatures of 241 °C at moderate salinity up to 7.3 eq. mass% NaCl (Fig. 11). Sulphide-sulphosalt quartz veins display an average homogenization temperature of 209 °C at low salinity averaging to 4.6 eq. mass% NaCl (Fig. 11). Inclusions in dolomite veins yield interesting results, i.e. a wide range of homogenization temperature (190 to 387 °C, Fig. 10f) and variable densities of bulk inclusion (0.55 – 0.9 g/cm³). The salinity of inclusions in dolomite is relatively low (average of 3.1 eq. mass% NaCl, Fig. 11). This variability may reflect the gradual evolution of fluid trapping conditions in dolomite. Mineralized vein data are clustered and yield homogenization temperatures lower than 250 °C, whereas barren veins scatter (Fig. 10d–f).

The properties of fluid inclusion (i.e. volume fraction) and microthermometric data from different types of fluids and host minerals were used to construct the isochores with the program ISOC (Bakker, 2003). The isochores of the quartz pyrite – Au veins are slightly above those of the quartz sulphide- ± sulphosalt – Au veins. The estimated trapping conditions of the quartz pyrite – Au veins are at about 180–250 °C and < 1.27 kbar, which corresponds to a depth of 4.8 km (assuming lithostatic overburden). The quartz sulphide ± sulphosalt Au veins are at similar temperatures and slightly lower pressures of less than 0.84 kbar (Fig. 14a). Both veins have similar dip directions and thus are parallel. The presence of minor amounts of CO₂ in inclusion type I results in flatter slopes which overlap with the quartz sulphide ± sulphosalt Au isochore field (Fig. 14a). The inferred trapping conditions of Type-II fluid inclusions in barren quartz-carbonate veins range from 374 °C and 1.15 kbar to 300 °C and 0.24 kbar (Fig. 14a). The parallel isochores may reflect a gradual evolution of trapping conditions for each fluid generation. Fluids are continuously trapped in quartz-carbonate during cooling and exhumation of the rock.

The fluid characteristics at Awak Mas District are similar to other gold deposit elsewhere, for example, the Racetrack deposit in the Yilgarn block of Western Australia is an example of a shallow orogenic gold system deposited from CO₂-poor fluids in lower greenschist-facies rocks at depths < 2.5 km. This deposit has hydrothermal alteration similar to orogenic deposits, whereas the quartz-vein texture and the ore mineralogy are more characteristic of epithermal deposits (Gebremariam et al., 1993). The ore mineralogy consists of arsenopyrite, pyrite, chalcopyrite, sphalerite, galena, freibergite, tetrahedrite, tennantite, electrum and gold, with fluid salinity of 1–8 (average 4 eq% NaCl), CO₂ content of < 0.85 molal and homogenization temperatures ranging from 190 to 260 °C. Similar textures were described from the Wiluna deposits; there, δ¹⁸O_{quartz} of 4.4‰ ± 2.3‰ relative to SMOW indicates contribution of near-surface waters in an orogenic gold

deposit (Hagemann et al., 1994).

6.3. Interpretation of halogen data

The halogen ratios (Cl/Br/I) can be used to detect sources of salinity, fluid mixing relations and water-rock reactions, because halogens are strongly fractionated by evaporation and organic activity (Böhlke and Irwin, 1992). Literature data have been plotted as fields for comparison (Fig. 12).

In Fig. 12a, the values of I/Cl versus Br/Cl are plotted for all investigated samples. The log Br/Cl values of the gold deposits in Latimojong (–3.38 to 2.51) overlap with the ore fluids circulating in orogenic deposits of Brusson, NW Italy (Yardley, 1993), Mokrsko, Bohemian Massif (Boiron et al., 2001) and Laurie'ras, French Massif Central (Boiron et al., 2003). Data overlap only somewhat at the low end of their range with the magmatic deposits in SW England (Böhlke and Irwin, 1992) and with MORB fields (Kendrick et al., 2012).

The Na/Cl/Br diagrams based on Landis and Hofstra (2012) demonstrate that the halogen data of Latimojong scatter over a large range and plot into several fields (Fig. 12b). They are similar to metamorphic fluids from Phanerozoic orogenic gold deposit with some data shifting into the albitization field (blue arrow, Fig. 12b). The introduction of sodium-rich minerals through an albitization process may be regarded as metasomatic alteration during the cooling process and metal deposition. Data points also differ from residual evaporative brines of Mississippi Valley-type (MVT) Pb-Zn deposits (light blue); therefore, dissolution or precipitation of halite are considered to be less important factors in the present study (Landis and Hofstra, 2012).

The Br/Cl diagram (Fig. 12c) supports the evidence of different fluid sources in the Latimojong Metamorphic Complex. The Br/Cl values from this study are comparable to orogenic gold deposits of Otago schist, New Zealand (Goodwin, 2010), Muruntau, Uzbekistan (Graupner et al., 2006) and porphyry Cu deposits in USA (Kendrick et al., 2001). By contrast, the values are different to carbonate-hosted Zn-Pb deposits in Poland (Heijnen et al., 2003) and the Baia Mare epithermal gold polymetallic district, Romania (Grancea et al., 2002).

It is suggested that there is no contribution of the Neogene intrusive rocks in Western Sulawesi to the gold mineralization, as the halogen data (Fig. 12a and c) do not indicate magmatic sources. It is inferred that the halogen ratios of fluids trapped within quartz grains are in agreement with metamorphic fluids, which probably mixed with meteoric water. Metamorphic reactions in the metasedimentary rocks during the retrogression stage are considered as the main source of ascending fluids for the formation of the economic gold mineralization at Latimojong.

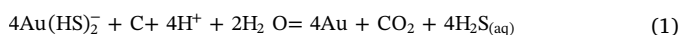
While single inclusion analysis always is preferable, bulk analytical methods are sufficiently sensitive for many ions and halogens of interest. Bulk extraction techniques suffers from several complications: (i) solid inclusions can interfere with the signal from fluid inclusions, (ii) leaching larger sample volumes yields results from multiple, possibly unrelated fluid inclusion generations (Banks and Yardley, 1992). Therefore, the results of this study must be checked further using laser ablation techniques, or by the selection of crystals with only one type of fluid inclusions.

6.4. Gold transport and precipitation mechanism

In a system with a temperatures lower than 350 °C, gold solubility is mostly controlled by the bisulphide ion (HS[–]) with AuHS⁰ predominating at lower pH and Au(HS)₂[–] at higher pH (Gammons and Williams-Jones, 1997). At temperatures higher than 350 °C, gold mostly occurs as AuCl₂[–] species. Based on the homogenization temperatures obtained in this study, the bisulphide complex (HS[–]) is considered as the main ligand for gold deposition in the Latimojong Metamorphic Complex. Mineral assemblages and fluid inclusion composition within Awak mas and Salu Bullo are consistent with a relatively reduced fluid.

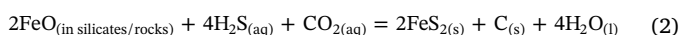
The halogen data of fluid inclusions from Awak Mas and Salu Bullo are comparable to other gold deposits formed by fluid-mixing between deeply sourced fluids with some contribution of shallow water (meteoric water), i.e. gold deposits in the Variscan belt of western Europe (Boiron et al., 2003) and epizonal orogenic gold deposits in Western Australia (i.e. Wiluna and Racetrack gold deposits, Hagemann et al., 1992). Mikucki (1998) suggested that phase separation and fluid mixing reactions also appear as an effective gold depositional mechanism in shallow Archean orogenic gold deposits. Other mechanisms for gold precipitation from hydrothermal ore fluids include (i) pressure-temperature changes, (ii) interaction between ore fluids and surrounding host rocks, (iii) phase separation in response to decreasing pressures during the rise of the ore fluid, or (iv) mixing of two or more different fluids (Mikucki, 1998).

Mineralized quartz veins in Awak Mas and Salu Bullo are related to major structures, including shear-zone, extensional veins and breccia veins. Gold grains are observed locally in pyrite grains within graphite rich layer (carbonaceous phyllite, i.e. sample A198-241) and iron-rich host rock (hematitic mudstone, i.e. sample S69-25). The presence of carbonaceous material in metasedimentary host rocks may have acted as a reducing agent for fluid carrying gold as bisulphide complexes, resulting in gold precipitation via reaction (1) (Hu et al., 2015):



Carbonaceous materials may also be deposited from hydrothermal fluids containing volatile organic compounds during gold deposit formation. Hydrothermal carbonaceous materials precipitate from fluids with sulphides via reaction (2), causing loss of sulphur from solution which results in gold deposition via destabilization of aqueous Au-sulphide complexes.

Rocks with high Fe/Fe + Mg are good traps for epigenetic gold, i.e. iron formations, iron-rich tholeiites in Archean greenstone belts, and felsic igneous rock types, because iron forms as an important ore sink during desulphidation reactions with the gold-transporting fluids (Goldfarb et al., 2005). This observation is similar to the observation in the Awak Mas District, where some gold grains are trapped within hydrothermal pyrite in hematitic mudstone (Fig. 3c).



The evidence from crush leach analyses, the intimate association between high gold grades and carbonaceous/iron-bearing host rocks highlight the fact that the fluid mixing, fluid-wallrock interaction and wallrock sulphidation are the most important mechanisms in precipitating gold from solution in the Awak Mas and Salu Bullo gold deposits.

6.5. Ore deposit type

The Awak Mas District is characterized by low silver contents in gold (gold fineness ranging from 842 to 936, average of 907, $n = 87$) (Hakim, 2017; Hakim and Melcher, 2016a; Harjanto et al., 2016b) and these ratios do not change significantly with depth, unlike in epithermal gold deposits. Gold of lower fineness commonly forms at shallow epithermal levels (Corbett and Leach, 1998; White, 1981). By contrast, gold deposited under low pH conditions will have a high fineness, similar to the high sulphidation deposits in the southwest Pacific (Leach and Corbett, 2008).

The ore mineralogy at Awak Mas mainly consists of pyrite, chalcopyrite and galena with minor tetrahedrite-tennantite. The proximal alteration is mainly albite and silica whereas most distal alteration is represented by secondary chlorite, calcite and lacks hydrothermal sulphide minerals. Although some minerals (i.e. covellite, enargite/luzonite) are typical of epithermal mineralization, their typical alteration assemblages (i.e. high-sulphidation: alunite, barite, kaolinite, diapore, pyrophyllite; low-sulphidation: adularia, illite) are absent (Hakim et al., 2017).

Depth and pressure estimation are the major evidence arguing against an epithermal style. Epithermal ores form in a shallow environment under low pressure, from the surface to as deep as 2 km and pressures at about 0.5 kbar (Cooke and Simmons, 2000; Corbett and Leach, 1998; Gemmill and Simmons, 2007; White and Hedenquist, 1995). By contrast, the mineralizing veins at Awak Mas District formed at about 4.8 km (see Section 6.2). Considering that pressures and depths of ore deposition exceed 0.5 kbar and 2 km, gold deposits in the Awak Mas District are not comparable to the epithermal style. Moderate salinity of fluid inclusions (3–8 eq. wt% NaCl, average of 5 eq. wt% NaCl) and the presence of aqueous-carbonic inclusions ($\text{CO}_2 \pm \text{N}_2$) are diagnostic features for orogenic gold systems and reflect a near-neutral pH, reduced environment, low-salinity $\text{H}_2\text{O}-\text{CO}_2$ fluids with arsenic as minor constituents. They represent fluids that are able to mobilize gold under greenschist-facies conditions. Halogen data (Br/Cl/1 ratios) for hydrothermal ore fluids at Awak Mas District are in agreement with metamorphic fluids (this study and Harjanto et al., 2016b) with little or no magmatic signature.

The results of in situ laser ablation-inductively coupled mass spectrometry and electron microprobe analyses for different types of pyrite provide evidence for trace element enrichment of Co, Ni, As and low Cu, Zn, Se, Bi, Au, Ag (Hakim 2017). Cobalt, nickel and arsenic enrichment in pyrite may indicate that these elements are available during particular phases of metamorphism (Craig, 2001).

A number of features at the Awak Mas District thus provide evidence that the gold deposits within belong to the epizonal orogenic gold group (Groves et al., 1998). This epizonal level of orogenic gold emplacement is consistent with the high As-Sb concentrations, the dominance of brittle structures and the open-space filling textures (Goldfarb et al., 2005).

6.6. Mineralization related to metamorphism and genetic model

The Awak Mas District is hosted in rocks metamorphosed from blueschist- to greenschist-facies conditions. The mineralization history of Awak Mas is comparable to gold deposits in the Otago and Alpine schists, New Zealand. The maximum pressure and temperature of metamorphism for the Otago schists are estimated at 450 °C and between 4.5 and 8 kbar (Pitcairn et al., 2010), and locally, amphibolite-facies conditions have been reached. In comparison, the Latimojong Metamorphic Complex underwent pressure-dominated pumpellyite-actinolite to greenschist-facies metamorphism. We have observed an orthogneiss boulder (± 2 m in diameter) in the detachment zone of LMC and Lamasi Complex (coordinates S3°20'08.8" E120°07'59.5"), however, high-grade metamorphic rocks are not present in the drill hole samples at Awak Mas District. The orthogneiss has green porphyroclasts (probably amphibole) and shows a ductile texture, and is underlain by metavolcanic rocks within the ophiolite unit. Our field observations suggest that the orthogneiss probably represents a metamorphic sole of the Lamasi Complex, which was obducted onto the metamorphic complex. Alternatively, White et al. (2017) suggested that the metaigneous rocks (i.e. amphibolites, meta-gabbro and meta granitoids) were tectonically juxtaposed within parts of the LMC and represent younger rocks.

Prograde metamorphism of sedimentary rocks has been shown to mobilize elements, including Au and As, to form world-class orogenic gold deposits, such as in the metasedimentary schist belt of southern New Zealand (Large et al., 2011; Pitcairn et al., 2006). The trace elements were released from those rocks into metamorphic fluids that are generated by metamorphic dehydration reactions (Large et al., 2011). These authors considered that carbonaceous metasedimentary rocks are required to form large deposits in metasedimentary host rocks (Carlin-type and orogenic gold deposits), where gold and arsenic are introduced early into black shale and turbidites during sedimentation and diagenesis, and later concentrated to ore grade by hydrothermal, tectonic or magmatic processes.

Pitcairn et al. (2015) evaluated the effects of increasing metamorphic grade on the concentration of Au and related elements (As, Sb, Se and Hg) in metabasaltic samples in the Otago and Alpine schists, New Zealand. The results prove that metasedimentary rocks are more suitable source rocks for fluids and metals in orogenic gold deposits than metabasaltic rocks, as they show mobility during metamorphism of all elements commonly enriched in this style of deposit.

We propose the following model for the gold mineralization for the Awak Mas District:

The Late Cretaceous LMC may have experienced high-pressure low-temperature metamorphism during the subduction of Indo-Australian plate into the Sundaland Craton (Bergman et al., 1996; Parkinson et al., 1998; van Leeuwen and Muhardjo, 2005; White et al., 2017). This high-pressure metamorphism caused limited fluid circulation, the breakdown of volatile-bearing minerals and the release of water rich fluid, followed by cooling and isothermal decompression to a maximum of 3 kbar (based on the ore fluids isochores, Fig. 14a), giving rise to gold precipitation. Gold and arsenic were mobile during regional metamorphism (Pitcairn et al., 2006) and the brittle faults acted as fluid conduits for ore precipitation at shallow depth during retrogression. Metamorphic reactions in the metasedimentary rocks during the retrogression stage are considered as the main source of ascending metamorphic fluids to form the Au-mineralization at Latimojong (Fig. 14b). More support for this is provided by $\delta^{18}\text{O}$ values of 17.9‰ and 20.6‰ obtained from mineralized quartz veins at Awak Mas deposit (Harjanto et al., 2016a), which was interpreted as fluids from metamorphic de-watering reactions.

During the retrogression stage, hydrothermal alteration affected large volumes of rocks; therefore, most rocks studied are hydrothermally altered. This observation is based on the mineralogy of host rocks, which indicates typical greenschist facies mineral assemblages of quartz + albite + calcite \pm chlorite \pm sphene. The pumpellyite – actinolite facies is observed only in more mafic host rocks, with mineral assemblages of Pmp + Act + Chl + Ep + Cal \pm Spn \pm Qz, sometimes with relic clinopyroxene. The rocks of the Lamasi Complex are unmineralized with gold, and we therefore suspect that the mineralization must be earlier than the obduction and/or movement of these rocks onto the metamorphic basement. If the mineralization took place later than the obduction of ophiolite and the Lamasi Complex acted as a barrier for mineralizing fluids, we would expect vein system at the contact between the metamorphic complex and the Lamasi Complex.

Archibald et al. (1996) in van Leeuwen and Pieters (2011) inferred that the flysch sequence in the Awak Mas district is unlikely to be a source of the gold owing to the low gold contents generally inherent to this sediment type. Those authors suggested that the source of fluids in Latimojong is the basement blueschists and associated serpentinites and/or adjacent ophiolites, where intense albite metasomatism accompanied by low- to moderate-temperature seafloor hydrothermal alteration is inferred to have leached the gold from the basaltic-gabbroic rocks (Archibald et al., 1996). Those authors postulated that the gold mineralization took place between 8 and 6 Ma, which is based on cross-cutting relationships, radiometric dating and superimposition of fluid temperatures on fission track uplift curve data from Bergman et al. (1996).

Intrusion-related gold (IRG) has been suggested as an alternative scenario for the mineralization at the Awak Mas District (Meyer, 2016; van Leeuwen and Pieters, 2011). van Leeuwen and Pieters (2011) suggest that Mid-Miocene extension and an associated heating event were the main fluid drivers for gold mobilization, followed by deposition during uplift. Meyer (2016) reviews several orogenic gold mineralization in the world, including the Awak Mas deposit. Based on the spatial-temporal associations with granitoids and oxygen-sulphur isotope data of Harjanto (2017), Meyer (2016) inferred that melts and fluids were both inherent products of thermal events during orogenic processes and suggests that the mineralization history in the Awak Mas District is not directly related to regional metamorphism.

Despite this controversy, there are no earlier reports on the relative timing of gold mineralization to the structural evolution in the studied area. The timing of mineralization can potentially be dated using radioactive minerals, including monazite, xenotime and zircon. In the Awak Mas and Salu Bullo deposits, monazite is abundant, whereas xenotime, baddeleyite and rutile are minor. Those minerals are associated with mineralized ore veins, and have irregular grain shapes. The size of minerals is generally less than 30 μm in diameter; therefore, mineral separation is needed for age dating. In-situ geochronological investigations on these minerals should provide more clarity about the timing of mineralization.

7. Conclusions

Petrographical, mineralogical, and geochemical methods have been used to construct the genetic model for gold mineralization hosted by metasedimentary and metavolcanic rocks in the Latimojong Metamorphic Complex. Different geothermometers (chlorite, cation leachates and carbonaceous material) applied are consistent with the results obtained using microthermometric techniques. The results of this study indicate that the formation temperature is comparable with metamorphic temperatures of the greenschist facies.

Gold deposits formed from $\text{H}_2\text{O}-\text{CO}_2-\text{NaCl}$ (type I) and $\text{H}_2\text{O}-\text{NaCl}$ (type II, type III) fluids. The estimated trapping conditions of the gold are between 180 and 250 $^\circ\text{C}$ at pressures of 0.84 to 1.3 kbar. Trapping conditions of the barren veins are at about 300–374 $^\circ\text{C}$ and < 1.15 kbar. The fluid pressure estimation corresponds to a depth lower than 5 km, assuming lithostatic conditions, providing evidence for epizonal gold mineralization. Considering the homogenization and salinity data, the bisulphide complex (HS^-) is considered as the main ligand for gold deposition. Halogen data (Br/Cl/I ratios) for hydrothermal ore fluids at Awak Mas District are in agreement with metamorphic fluids with little or no magmatic signature.

The high-pressure low-temperature metamorphism during the subduction processes caused limited fluid circulation, the breakdown of volatile-bearing minerals and the release of water rich fluid, followed by cooling and isothermal decompression, giving rise to gold precipitation. Metamorphic reactions in the metasedimentary rocks during the retrogression stage are considered as the main source of ascending metamorphic fluids to form the Au-mineralization at Latimojong. In addition, the accretionary complex may also have contributed in several ways to the formation of the mineralization as favourable host and/or as a driver of fluid generation during the retrograde stage of metamorphism.

Acknowledgements

We thank the mining company PT Masmino Dwi Area, Indonesia for their help during field work. Analytical help from Federica Zaccarini, Maik Zimmermann and sample preparation by Sabine Feuchter are much appreciated. The authors wish to acknowledge two reviewers Greg Corbett and Theo van Leeuwen for their constructive criticism of various aspect of this manuscript. Research reported in this publication was supported by the ASEAN-European Academic University Network (ASEA-UNINET) as part of PhD research to the first author. Franco Pirajno is also thanked for editorial handling.

Appendix A. Supplementary data

Supplementary data associated with this article can be found, in the online version, at <http://dx.doi.org/10.1016/j.oregeorev.2018.05.001>.

References

- Anderko, A., Pitzer, K.S., 1993. Equation-of-state representation of phase equilibria and volumetric properties of the system $\text{NaCl}-\text{H}_2\text{O}$ above 573 K. *Geochimica et*

- Cosmochimica Acta 57 (8), 1657–1680. [http://dx.doi.org/10.1016/0016-7037\(93\)90105-6](http://dx.doi.org/10.1016/0016-7037(93)90105-6).
- Archibald, N.J., Power, W.L., Ketelaar, P.B., Utley, D.C., Panizza, N., Nicholas, S., 1996. Geology of the Awak Mas prospect area, South Central Sulawesi, Indonesia. Report prepared for PT Masmindio Eka Sakti.
- Bakker, R.J., 1997. Clathrates: computer programs to calculate fluid inclusion V-X properties using clathrate melting temperatures. *Comput. Geosci.* 23 (1), 1–18. [http://dx.doi.org/10.1016/S0098-3004\(96\)00073-8](http://dx.doi.org/10.1016/S0098-3004(96)00073-8).
- Bakker, R.J., 2003. Package FLUIDS 1. Computer programs for analysis of fluid inclusion data and for modelling bulk fluid properties. *Chem. Geol.* 194 (1–3), 3–23. [http://dx.doi.org/10.1016/S0009-2541\(02\)00268-1](http://dx.doi.org/10.1016/S0009-2541(02)00268-1).
- Bakker, R.J., Diamond, L.W., 2006. Estimation of volume fractions of liquid and vapor phases in fluid inclusions, and definition of inclusion shapes. *Am. Mineral.* 91 (4), 635–657. <http://dx.doi.org/10.2138/am.2006.1845>.
- Banks, D., Gleeson, S., Green, R., 2000. Determination of the origin of salinity in granite-related fluids: Evidence from chlorine isotopes in fluid inclusions. *J. Geochem. Explor.* 69–70, 309–312. [http://dx.doi.org/10.1016/S0375-6742\(00\)00076-5](http://dx.doi.org/10.1016/S0375-6742(00)00076-5).
- Banks, D., Yardley, B., 1992. Crush-leach analysis of fluid inclusions in small natural and synthetic samples. *Geochim. Cosmochim. Acta* 56 (1), 245–248. [http://dx.doi.org/10.1016/0016-7037\(92\)90129-7](http://dx.doi.org/10.1016/0016-7037(92)90129-7).
- Barton Jr., P.B., Bethke, P.M., 1987. Chalcopyrite disease in sphalerite: Pathology and epidemiology. *Am. Mineral.* 72 (5–6), 451–467.
- Beiersdorfer, R.E., Day, H.W., 1995. Mineral paragenesis of pumpellyite in low-grade mafic rocks. In: Schiffman, P., Day, H.W. (Eds.), *Low-grade Metamorphism of Mafic Rocks*, vol. 296. Geological Society of America, Boulder, Colo., pp. 5–28.
- Bergman, S.C., Coffield, D.Q., Talbot, J.P., Garrard, R.A., 1996. Tertiary tectonic and magmatic evolution of western Sulawesi and the Makassar Strait, Indonesia: evidence for a Miocene continent-continent collision. *Geol. Soc. London Spec. Publ.* 106 (1), 391–429. <http://dx.doi.org/10.1144/GSL.SP.1996.106.01.25>.
- Beysac, O., Goffé, B., Chopin, C., Rouzaud, J.N., 2002. Raman spectra of carbonaceous material in metasediments: a new geothermometer. *J. Metamorph. Geol.* 20 (9), 859–871. <http://dx.doi.org/10.1046/j.1525-1314.2002.00408.x>.
- Böhlke, J., Irwin, J., 1992. Laser microprobe analyses of Cl, Br, I, and K in fluid inclusions: Implications for sources of salinity in some ancient hydrothermal fluids. *Geochimica et Cosmochimica Acta* 56 (1), 203–225. [http://dx.doi.org/10.1016/0016-7037\(92\)90127-5](http://dx.doi.org/10.1016/0016-7037(92)90127-5).
- Boiron, M.-C., Barakat, A., Cathelineau, M., Banks, D.A., Durisová, J., Morávek, P., 2001. Geometry and P–V–T–X conditions of microfissural ore fluid migration: the Mokrosko gold deposit (Bohemia). *Chem. Geol.* 173 (1–3), 207–225. [http://dx.doi.org/10.1016/S0009-2541\(00\)00276-X](http://dx.doi.org/10.1016/S0009-2541(00)00276-X).
- Boiron, M.-C., Cathelineau, M., Banks, D.A., Fourcade, S., Vallance, J., 2003. Mixing of metamorphic and surficial fluids during the uplift of the Hercynian upper crust: consequences for gold deposition. *Chem. Geol.* 194 (1–3), 119–141. [http://dx.doi.org/10.1016/S0009-2541\(02\)00274-7](http://dx.doi.org/10.1016/S0009-2541(02)00274-7).
- Bourdelle, F., Cathelineau, M., 2015. Low-temperature chlorite geothermometry: a graphical representation based on a T-R²–Si diagram. *Eur. J. Mineral.* 27 (5), 617–626. <http://dx.doi.org/10.1127/ejm/2015/0027-2467>.
- Cooke, D.R., Simmons, S.F., 2000. Characteristics and genesis of epithermal gold deposits. *Rev. Econ. Geol.* 13, 221–244.
- Corbett, G.J., Leach, T.M., 1998. Southwest Pacific Rim gold-copper systems: Structure, alteration and mineralization. *Soc. Econ. Geol. Spec. Publ.* 6, 240.
- Craig, J.R., 2001. Ore-mineral textures and the tales they tell. *Can. Mineral.* 39 (4), 937–956. <http://dx.doi.org/10.2113/gscanmin.39.4.937>.
- Craw, D., 2002. Geochemistry of late metamorphic hydrothermal alteration and graphitisation of host rock, Macraes gold mine, Otago Schist, New Zealand. *Chem. Geol.* 191 (4), 257–275. [http://dx.doi.org/10.1016/S0009-2541\(02\)00139-0](http://dx.doi.org/10.1016/S0009-2541(02)00139-0).
- Craw, D., MacKenzie, D., 2016. *Macraes Orogenic Gold Deposit (New Zealand): Origin and Development of a World Class Gold Mine*. Springer, Switzerland, pp. 12783.
- Cube, 2017. Awak Mas and Salu Bullo Deposits Summary Reports – May 2017. Nusantara Resources.
- Djuri, Sudjatmiko, Bachri, S., Sukido, 1988. *Geological Map of the Majene and Western Part of the Palopo sheets (1:250,000)*. Geological Research and Development Centre, Bandung, Indonesia.
- Duan, Z., Möller, N., Weare, J.H., 1992a. An equation of state for the CH₄–CO₂–H₂O system: I. Pure systems from 0 to 1000 °C and 0 to 8000 bar. *Geochim. Cosmochim. Acta* 56 (7), 2605–2617. [http://dx.doi.org/10.1016/0016-7037\(92\)90347-L](http://dx.doi.org/10.1016/0016-7037(92)90347-L).
- Duan, Z., Möller, N., Weare, J.H., 1992b. An equation of state for the CH₄–CO₂–H₂O system: II. Mixtures from 50 to 1000 °C and 0 to 1000 bar. *Geochimica et Cosmochimica Acta* 56 (7), 2619–2631. [10.1016/0016-7037\(92\)90348-M](http://dx.doi.org/10.1016/0016-7037(92)90348-M).
- Duan, Z., Möller, N., Weare, J.H., 1995. Equation of state for the NaCl–H₂O–CO₂ system: prediction of phase equilibria and volumetric properties. *Geochimica et Cosmochimica Acta* 59 (14), 2869–2882. [http://dx.doi.org/10.1016/0016-7037\(95\)00182-4](http://dx.doi.org/10.1016/0016-7037(95)00182-4).
- Force, E.R. (Ed.), 1991. *Geology of Titanium-mineral Deposits*. Geological Society of America, Boulder, Colo.
- Gammons, C.H., Williams-Jones, A.E., 1997. Chemical mobility of gold in the porphyry-epithermal environment. *Econ. Geol.* 92 (1), 45–59. <http://dx.doi.org/10.2113/gsecongeo.92.1.45>.
- Garwin, S., Hall, R., Watanabe, Y., 2005. Tectonic setting, geology, and gold and copper mineralization in Cenozoic magmatic arcs of Southeast Asia and the West Pacific. *Economic Geology 100th Anniversary Volume*, 891–900.
- Gebre-Mariam, M., Groves, D.I., McNaughton, N.J., Mikucki, E.J., Vearncombe, J.R., 1993. Archaean Au–Ag mineralization at Racetrack, near Kalgoolie, Western Australia: a high crustal-level expression of the Archaean composite lode-gold system. *Mineral. Deposita* 28 (6), 375–387. <http://dx.doi.org/10.1007/BF02431597>.
- Gemmell, J.B., Simmons, S.F., 2007. A group of papers devoted to epithermal Au–Ag deposits: preface. *Econ. Geol.* 102 (5), 783. <http://dx.doi.org/10.2113/gsecongeo.102.5.783>.
- Giggenbach, W.F., 1988. Geothermal solute equilibria. Derivation of Na–K–Mg–Ca geothermometers. *Geochimica et Cosmochimica Acta* 52 (12), 2749–2765. [http://dx.doi.org/10.1016/0016-7037\(88\)90143-3](http://dx.doi.org/10.1016/0016-7037(88)90143-3).
- Gleeson, S.A., 2003. Bulk analyses of electrolytes in fluid inclusions: In: Samson, I., Anderson, A., Marshall, D. (Eds.), *Fluid Inclusions: Analysis and Interpretation*. Mineralogical Association of Canada, Short Course 32, pp. 233–247.
- Goldfarb, R.J., Baker, T., Dube, B., Groves, D.I., Hart, C.J.R., Gosselin, P., 2005. Distribution, character, and genesis of gold deposits in metamorphic terranes. *Economic Geology 100th anniversary volume* 40.
- Goodwin, N.R.J., 2010. A combined noble gas and halogen study of orogenic gold mineralisation in the Alpine and Otago Schists, New Zealand.
- Grancea, L., Bailly, L., Leroy, J., Banks, D., Marcoux, E., Milési, J., Cuney, M., André, A., Istvan, D., Fabre, C., 2002. Fluid evolution in the Baia Mare epithermal gold/poly-metallic district, Inner Carpathians, Romania. *Mineralium Deposita* 37 (6–7), 630–647. <http://dx.doi.org/10.1007/s00126-002-0276-5>.
- Graupner, T., Niedermann, S., Kempe, U., Klemm, R., Bechtel, A., 2006. Origin of ore fluids in the Muruntau gold system: constraints from noble gas, carbon isotope and halogen data. *Geochimica et Cosmochimica Acta* 70 (21), 5356–5370. <http://dx.doi.org/10.1016/j.gca.2006.08.013>.
- Groves, D., Goldfarb, R., Gebre-Mariam, M., Hagemann, S., Robert, F., 1998. Orogenic gold deposits: a proposed classification in the context of their crustal distribution and relationship to other gold deposit types. *Ore Geol. Rev.* 13 (1–5), 7–27. [http://dx.doi.org/10.1016/S0169-1368\(97\)00012-7](http://dx.doi.org/10.1016/S0169-1368(97)00012-7).
- Gu, X.X., Zhang, Y.M., Li, B.H., Dong, S.Y., Xue, C.J., Fu, S.H., 2012. Hydrocarbon- and ore-bearing basinal fluids: a possible link between gold mineralization and hydrocarbon accumulation in the Youjiang basin, South China. *Miner. Deposita* 47 (6), 663–682. <http://dx.doi.org/10.1007/s00126-011-0388-x>.
- Hagemann, S.G., Gebre-Mariam, M., Groves, D.I., 1994. Surface-water influx in shallow-level Archean lode-gold deposits in Western, Australia. *Geology* 22 (12), 1067. [http://dx.doi.org/10.1130/0091-7613\(1994\)022<1067:SWIISL>2.3.CO;2](http://dx.doi.org/10.1130/0091-7613(1994)022<1067:SWIISL>2.3.CO;2).
- Hagemann, S.G., Groves, D.I., Ridley, J.R., Vearncombe, J.R., 1992. The Archean lode gold deposits at Wiluna, Western Australia; high-level brittle-style mineralization in a strike-slip regime. *Econ. Geol.* 87 (4), 1022–1053. <http://dx.doi.org/10.2113/gsecongeo.87.4.1022>.
- Hakim, A.Y.A., 2017. *Genesis of Orogenic Gold in the Latimojong District, South Sulawesi, Indonesia* (Ph.D. thesis). Montanuniversität Leoben, Austria, pp. 355.
- Hakim, A.Y.A., Melcher, F., 2015. Mineralogical study of the Awak Mas Deposit: a Contribution to the Ore Genesis of Disseminated Gold Deposits in South Celebes, Indonesia. *Mitteilungen der Österreichischen Mineralogischen Gesellschaft* 161, 43 (abstract).
- Hakim, A.Y.A., Melcher, F., 2016a. The composition of gold and mercurian rich tetra-hedrite from the sedimentary hosted disseminated gold in Latimojong mountain, South Sulawesi, Indonesia. 1st Postgraduate conference on Geology of Ore Deposits. Freiberg 1, 12 (abstract).
- Hakim, A.Y.A., Melcher, F., 2016b. The Sallu Bulu Mesothermal Gold Deposit in South Sulawesi, Indonesia. *GeoTiro 2016*, 98 (abstract).
- Hakim, A.Y.A., Melcher, F., 2017a. Magmatic chromian spinel in metabasite from the Latimojong Mountains, Sulawesi, Indonesia. *Mitteilungen der Österreichischen Mineralogischen Gesellschaft* 163, 42 (abstract).
- Hakim, A.Y.A., Melcher, F., 2017b. Timing of mineralization and origin of hydrothermal carbonate at the gold deposits within the Latimojong Complex, Indonesia. 2nd Postgraduate conference on Geology of Ore Deposits. Hannover 2, 22 (abstract).
- Hakim, A.Y.A., Melcher, F., Prochaska, W., Bakker, R.J., Rantitsch, G., 2017. The origin and evolution of fluids associated with gold deposits in the basement of Sulawesi, Indonesia. *Proceedings of the 14th SGA Biennial Meeting*, 20–23 August 2017, Québec City, Canada, 355–358.
- Hall, R., Wilson, M., 2000. Neogene sutures in eastern Indonesia. *J. Asian Earth Sci.* 18 (6), 781–808. [http://dx.doi.org/10.1016/S1367-9120\(00\)00040-7](http://dx.doi.org/10.1016/S1367-9120(00)00040-7).
- Harjanto, E., 2017. Hydrothermal alteration and gold mineralization of the Awak Mas gold deposit, Sulawesi Island, Indonesia. Mainz, G, Aachen, 200 Seiten.
- Harjanto, E., Meyer, F.M., Idrus, A., 2015. Geology and mineralization of Awak Mas gold deposit and challenges for new exploration targeting in the metamorphic rock terrain of eastern Indonesia. In: *Proceeding of the 13th Biennial SGA Meeting*, Nancy, France.
- Harjanto, E., Meyer, F.M., Idrus, A., 2016a. Hydrothermal alteration and gold mineralization of the meta-sedimentary rock hosted gold deposit Awak Mas, Sulawesi Island, Indonesia. In: *Proceeding of the 35th International Geological Congress*. Cape Town, South Africa.
- Harjanto, E., Meyer, F.M., Idrus, A., Widyandarko, H., Endrasari, N.L., 2016b. An update of key characteristics of Awak Mas mesothermal gold deposit, Sulawesi Island, Indonesia. *MGEI Annual Meeting 2016*. 4–6 October 2016.
- Heijlen, W., Muchez, P., Banks, D.A., Schneider, J., Kucha, H., Keppens, E., 2003. Carbonate-hosted Zn–Pb deposits in Upper Silesia, Poland: origin and evolution of mineralizing fluids and constraints on genetic models. *Econ. Geol.* 98 (5), 911–932. <http://dx.doi.org/10.2113/gsecongeo.98.5.911>.
- Hu, S., Evans, K., Craw, D., Rempel, K., Bourdet, J., Dick, J., Grice, K., 2015. Raman characterization of carbonaceous material in the Macraes orogenic gold deposit and metasedimentary host rocks, New Zealand. *Ore Geol. Rev.* 70, 80–95. <http://dx.doi.org/10.1016/j.oregeorev.2015.03.021>.
- Kadarusman, A., Miyashita, S., Maruyama, S., Parkinson, C.D., Ishikawa, A., 2004. Petrology, geochemistry and paleogeographic reconstruction of the East Sulawesi Ophiolite, Indonesia. *Tectonophysics* 392 (1–4), 55–83. <http://dx.doi.org/10.1016/j.tecto.2004.04.008>.
- Kendrick, M.A., Burgess, R., Patrick, R., Turner, G., 2001. Fluid inclusion noble gas and

- halogen evidence on the origin of Cu-Porphyry mineralising fluids. *Geochim. Cosmochim. Acta* 65 (16), 2651–2668. [http://dx.doi.org/10.1016/S0016-7037\(01\)00618-4](http://dx.doi.org/10.1016/S0016-7037(01)00618-4).
- Kendrick, M.A., Woodhead, J.D., Kamenetsky, V.S., 2012. Tracking halogens through the subduction cycle. *Geology* 40 (12), 1075–1078. <http://dx.doi.org/10.1130/G33265.1>.
- Kharaka, Y.K., Mariner, R.H., 1989. Chemical geothermometers and their application to formation waters from sedimentary basins. In: Nancy, D.N., McCulloh, T.H. (Eds.), *Thermal History of Sedimentary Basins. Methods and Case Histories*, pp. 99–117. 10.1007/978-1-4612-3492-0_6.
- Kranidiotis, P., MacLean, W.H., 1987. Systematics of chlorite alteration at the Phelps Dodge massive sulfide deposit, Matagami, Quebec. *Econ. Geol.* 82 (7), 1898–1911. <http://dx.doi.org/10.2113/gsecongeo.82.7.1898>.
- Kwieceńska, B., Petersen, H., 2004. Graphite, semi-graphite, natural coke, and natural char classification—ICCP system. *Int. J. Coal Geol.* 57 (2), 99–116. <http://dx.doi.org/10.1016/j.coal.2003.09.003>.
- Landis, G.P., Hofstra, A.H., 2012. Ore genesis constraints on the Idaho Cobalt Belt from fluid inclusion gas, noble gas isotope, and ion ratio analyses. *Econ. Geol.* 107 (6), 1189–1205. <http://dx.doi.org/10.2113/econgeo.107.6.1189>.
- Large, R.R., Bull, S.W., Maslennikov, V.V., 2011. A carbonaceous sedimentary source-rock model for carlin-type and orogenic gold deposits. *Econ. Geol.* 106 (3), 331–358. <http://dx.doi.org/10.2113/econgeo.106.3.331>.
- Leach, T.M., Corbett, G.J., 2008. Fluid mixing as a mechanism for bonanza grade epithermal gold formation. Paper presented at the Terry Leach Symposium.
- Liou, J.G., Maruyama, S., Cho, M., 1987. Very low-grade metamorphism of volcanic and volcanoclastic rocks-mineral assemblages and mineral facies: Low temperature metamorphism. Blackie and Son, London.
- Lünsdorf, N.K., 2015. Geothermometry by Raman Spectroscopy of Dispersed Organic Matter (Ph.D. thesis). University Göttingen.
- Lünsdorf, N.K., Dunkl, I., Schmidt, B.C., Rantitsch, G., von Eynatten, H., 2014. Towards a higher comparability of geothermometric data obtained by Raman spectroscopy of carbonaceous material. Part I: evaluation of biasing factors. *Geostand Geoanal. Res.* 38 (1), 73–94. <http://dx.doi.org/10.1111/j.1751-908X.2013.12011.x>.
- Lünsdorf, N.K., Dunkl, I., Schmidt, B.C., Rantitsch, G., von Eynatten, H., 2017. Towards a higher comparability of geothermometric data obtained by Raman spectroscopy of carbonaceous material. Part 2: a revised geothermometer. *Geostand Geoanal. Res.* 172 (Suppl. 1), 617. <http://dx.doi.org/10.1111/ggr.12178>.
- Lünsdorf, N.K., Lünsdorf, J.O., 2016. Evaluating Raman spectra of carbonaceous matter by automated, iterative curve-fitting. *Int. J. Coal Geol.* 160–161, 51–62. <http://dx.doi.org/10.1016/j.coal.2016.04.008>.
- Massonne, H.-J., Schreyer, W., 1987. Phengite geobarometry based on the limiting assemblage with K-feldspar, phlogopite, and quartz. *Contr. Mineral. Petrol.* 96 (2), 212–224. <http://dx.doi.org/10.1007/BF00375235>.
- Maulana, A., Christy, A.G., Ellis, D.J., Imai, A., Watanabe, K., 2013. Geochemistry of eclogite- and blueschist-facies rocks from the Bantimala Complex, South Sulawesi, Indonesia: Protolith origin and tectonic setting. *Isl. Arc* 22 (4), 427–452. <http://dx.doi.org/10.1111/iar.12037>.
- Maulana, A., Imai, A., van Leeuwen, T., Watanabe, K., Yonezu, K., Nakano, T., Boyce, A., Page, L., Schersten, A., 2016. Origin and geodynamic setting of Late Cenozoic granitoids in Sulawesi, Indonesia. *J. Asian Earth Sci.* 124, 102–125. <http://dx.doi.org/10.1016/j.jseae.2016.04.018>.
- Meyer, F.M., 2016. Orogenic Gold Deposits-From Hypozonal to Epizonal Systems. Unconventional Exploration Target & Latest Technique and New Tools in Mineral and Coal Exploration MGEI 8th Annual Convention 2016, 15–18.
- Mikucki, E.J., 1998. Hydrothermal transport and depositional processes in Archean lode-gold systems: a review. *Ore Geol. Rev.* 13 (1–5), 307–321. [http://dx.doi.org/10.1016/S0169-1368\(97\)00025-5](http://dx.doi.org/10.1016/S0169-1368(97)00025-5).
- One Asia Resources, 2013. Awak Mas and Salu Bulu Gold Projects Sulawesi, Indonesia: Technical Report (unpublished report) by Tetra Tech.
- One Asia Resources, 2017. Awak Mas gold project resource update: Awak Mas and Salu Bulu Deposits Summary Report – May 2017: Mineral resource (JORC 2012) – 1.74 Moz new Geological Model.
- Parkinson, C., 1998. Emplacement of the East Sulawesi Ophiolite: evidence from sub-ophiolite metamorphic rocks. *J. Asian Earth Sci.* 16 (1), 13–28. [http://dx.doi.org/10.1016/S0743-9547\(97\)00039-1](http://dx.doi.org/10.1016/S0743-9547(97)00039-1).
- Parkinson, C.D., Miyazaki, K., Wakita, K., Barber, A.J., Carswell, D.A., 1998. An overview and tectonic synthesis of the pre-Tertiary very-high-pressure metamorphic and associated rocks of Java, Sulawesi and Kalimantan, Indonesia. *Isl. Arc* 7 (1–2), 184–200. <http://dx.doi.org/10.1046/j.1440-1738.1998.00184.x>.
- Peng, D.-Y., Robinson, D.B., 1976. A new two-constant equation of state. *Ind. Eng. Chem. Fund.* 15 (1), 59–64. <http://dx.doi.org/10.1021/i160057a011>.
- Pettijohn, F.J., Potter, P.E., Siever, R., 1987. *Sand and Sandstone*, second ed. Springer, New York, NY, pp. 553.
- Pitcairn, I.K., Craw, D., Teagle, D.A.H., 2015. Metabasalts as sources of metals in orogenic gold deposits. *Miner. Deposita* 50 (3), 373–390. <http://dx.doi.org/10.1007/s00126-014-0547-y>.
- Pitcairn, I.K., Olivo, G.R., Teagle, D.A.H., Craw, D., 2010. Sulfide evolution during prograde metamorphism of the otago and alpine schists, New Zealand. *Can. Mineral.* 48 (5), 1267–1295. <http://dx.doi.org/10.3749/canmin.48.5.1267>.
- Pitcairn, I.K., Roberts, S., Teagle, D.A.H., Craw, D., 2005. Detecting hydrothermal graphite deposition during metamorphism and gold mineralization. *J. Geol. Soc.* 162 (3), 429–432. <http://dx.doi.org/10.1144/0016-764904-139>.
- Pitcairn, I.K., Teagle, D.A.H., Craw, D., Olivo, G.R., Kerrich, R., Brewer, T.S., 2006. Sources of metals and fluids in orogenic gold deposits: insights from the Otago and Alpine Schists, New Zealand. *Econ. Geol.* 101 (8), 1525–1546. <http://dx.doi.org/10.2113/gsecongeo.101.8.1525>.
- Polve, M., Maury, R.C., Vidal, P., Priadi, B., Bellon, H., Soeria-Atmadja, R., Joron, J.-L., Cotten, J., 2001. Melting of lower continental crust in a young post-collision setting: a geochemical study of Plio-Quaternary acidic magmatism from central Sulawesi (Indonesia). *Bull. Soc. Geol. Fr.* 172 (3), 333–342. <http://dx.doi.org/10.2113/172.3.333>.
- Polvé, M., Maury, R.C., Bellon, H., Rangin, C., Priadi, B., Yuwono, S., Joron, J.L., Atmadja, R., 1997. Magmatic evolution of Sulawesi (Indonesia): Constraints on the Cenozoic geodynamic history of the Sundaland active margin. *Tectonophysics* 272 (1), 69–92. [http://dx.doi.org/10.1016/S0040-1951\(96\)00276-4](http://dx.doi.org/10.1016/S0040-1951(96)00276-4).
- Priadi, B., Polve, M., Maury, R.C., Bellon, H., Soeria-Atmadja, R., Joron, J.L., Cotten, J., 1994. Tertiary and quaternary magmatism in Central Sulawesi: chronological and petrological constraints. *J. SE Asian Earth Sci.* 9 (1–2), 81–93. [http://dx.doi.org/10.1016/0743-9547\(94\)90067-1](http://dx.doi.org/10.1016/0743-9547(94)90067-1).
- Querubin, C.D., Walters, S., 2012. Geology and Mineralization of Awak Mas: a sedimentary Hosted Gold Deposit, South Sulawesi, Indonesia. *Majalah Geologi Indonesia* 27 (2), 69–85.
- Rantitsch, G., Grogger, W., Teichert, C., Ebner, F., Hofer, C., Maurer, E.-M., Schaffer, B., Toth, M., 2004. Conversion of carbonaceous material to graphite within the Greywacke Zone of the Eastern Alps. *Int. J. Earth Sci. (Geol. Rundsch)* 93 (6), 959–973. <http://dx.doi.org/10.1007/s00531-004-0436-1>.
- Rantitsch, G., Lämmerer, W., Fisslthaler, E., Mitsche, S., Kaltenböck, H., 2016. On the discrimination of semi-graphite and graphite by Raman spectroscopy. *Int. J. Coal Geol.* 159, 48–56. <http://dx.doi.org/10.1016/j.coal.2016.04.001>.
- Soesilo, J., 1998. Metamorphism in the Latimojong Complex, South Sulawesi and its tectonic significances. Unpublished Magister thesis.
- Tuakia, M.Z., Takahashi, R., Imai, A., 2016. Fluid Inclusion and Sulfur Isotope Studies on the Salu Bulu Prospect, South Sulawesi, Indonesia: A Metasedimentary Rock-Hosted Gold Deposit. In: SEG 2016 Conference Tethyan Tectonics and Metallogeny.
- van Leeuwen, T.M., Muhandjo, 2005. Stratigraphy and tectonic setting of the Cretaceous and Paleogene volcanic-sedimentary successions in northwest Sulawesi, Indonesia: Implications for the Cenozoic evolution of Western and Northern Sulawesi. *J. Asian Earth Sci.* 25 (3), 481–511. <http://dx.doi.org/10.1016/j.jseae.2004.05.004>.
- van Leeuwen, T.M., Pieters, P.E., 2011. Mineral deposits of Sulawesi. In: *Proceedings of the Sulawesi Mineral Resources 2011*. 10.13140/2.1.3843.2322.
- van Leeuwen, T.M., Susanto, E.S., Maryanto, S., Hadiwisastra, S., Sudijono, Muhandjo, Prihardjo, 2010. Tectonostratigraphic evolution of Cenozoic marginal basin and continental margin successions in the Bone Mountains, Southwest Sulawesi, Indonesia. *J. Asian Earth Sci.* 38 (6), 233–254. <http://dx.doi.org/10.1016/j.jseae.2009.11.005>.
- Wakita, K., 2000. Cretaceous accretionary–collision complexes in central Indonesia. *J. Asian Earth Sci.* 18 (6), 739–749. [http://dx.doi.org/10.1016/S1367-9120\(00\)00020-1](http://dx.doi.org/10.1016/S1367-9120(00)00020-1).
- Wakita, K., Sopaheluwakan, J., Miyazaki, K., Zulkarnain, I., Munasri, 1996. Tectonic evolution of the Bantimala Complex, South Sulawesi, Indonesia. *Geol. Soc. London Spec. Publ.* 106 (1), 353–364. <http://dx.doi.org/10.1144/GSL.SP.1996.106.01.23>.
- White, D.E., 1981. Active geothermal systems and hydrothermal ore deposits. In: Skinner, B.J. (Ed.), *Seventy-Fifth Anniversary Volume. Economic Geology Publishing Company*.
- White, L.T., Hall, R., Armstrong, R.A., Barber, A.J., Fadel, M.B., Baxter, A., Wakita, K., Manning, C., Soesilo, J., 2017. The geological history of the Latimojong region of western Sulawesi. *J. Asian Earth Sci.* <http://dx.doi.org/10.1016/j.jseae.2017.02.005>.
- White, N.C., Hedenquist, J.W., 1995. Epithermal gold deposits: styles, characteristics and exploration. *SEG Newsletter* 23 (1), 9–13.
- Wyche, N.L., Eilu, P., Kopström, K., Kortelainen, V.J., Niiranen, T., Välimaa, J., 2015. The Suurikuisikko Gold Deposit (Kittilä Mine), Northern Finland. In: Maier, W.D., Lahtinen, R., O'Brien, H. (Eds.), *Mineral Deposits of Finland*. Elsevier, Amsterdam, Boston, pp. 411–433.
- Yardley, B.W.D., 1993. Post-Metamorphic Gold-Quartz Veins from N.W. Italy: the composition and origin of the ore fluid. *Mineral. Mag.* 57 (388), 407–422. <http://dx.doi.org/10.1180/minmag.1993.057.388.05>.